Draft version May 3, 2024
Typeset using LaTeX **twocolumn** style in AASTeX631

On Binary Formation from Three Initially Unbound Bodies

Dany Atallah,[1,2] Newlin C. Weatherford,[1,2] Alessandro A. Trani,[3,4,5] and Frederic A. Rasio[1,2]

[1] *Department of Physics & Astronomy, Northwestern University, Evanston IL 60208, USA*
[2] *Center for Interdisciplinary Exploration & Research in Astrophysics (CIERA), Evanston, IL*
[3] *Niels Bohr International Academy, Niels Bohr Institute, Blegdamsvej 17, 2100 Copenhagen, Denmark*
[4] *Research Center for the Early Universe, School of Science, The University of Tokyo, Tokyo 113-0033, Japan*
[5] *Okinawa Institute of Science and Technology, 1919-1 Tancha, Onna-son, Okinawa 904-0495, Japan*

ABSTRACT

We explore three-body binary formation (3BBF), the formation of a bound system via gravitational scattering of three initially unbound bodies (3UB), using direct numerical integrations. For the first time, we consider systems with unequal masses, as well as finite-size and post-Newtonian effects. Our analytically derived encounter rates and numerical scattering results reproduce the 3BBF rate predicted by Goodman & Hut (1993) for hard binaries in dense star clusters. We find that 3BBF occurs overwhelmingly through nonresonant encounters and that the two most massive bodies are never the most likely to bind. Instead, 3BBF favors pairing the two least massive bodies (for wide binaries) or the most plus least massive bodies (for hard binaries). 3BBF overwhelmingly favors wide binary formation with super-thermal eccentricities, perhaps helping to explain the eccentric wide binaries observed by Gaia. Hard binary formation is far rarer, but with a thermal eccentricity distribution. The semimajor axis distribution scales cumulatively as a^3 for hard and slightly wider binaries. Though mergers are rare between black holes when including relativistic effects, direct collisions occur frequently between main-sequence stars—more often than hard 3BBF. Yet, these collisions do not significantly suppress hard 3BBF at the low velocity dispersions typical of open or globular clusters. Energy dissipation through gravitational radiation leads to a small probability of a bound, hierarchical triple system forming directly from 3UB.

1. INTRODUCTION

The formation of binaries containing stellar and compact objects is essential to the production of numerous high-energy astrophysical phenomena, including gravitational wave emission and/or fast radio bursts released with compact object mergers (e.g., Rodriguez et al. 2019; Kremer et al. 2021), X-ray binaries (Sana et al. 2012), and supernovae (Maoz et al. 2014). Binaries are also essential to the evolution of dense stellar environments since they act as dynamical heat sources that expand the cluster's core through repeated scattering interactions—"binary burning" (e.g., Heggie & Hut 2003)—and promote stellar collisions and tidal disruption events (Bacon et al. 1996; Fregeau et al. 2004a; Ryu et al. 2023).

Many stellar binaries form 'primordially' in molecular clouds (e.g., Shu et al. 1987), but also dynamically from two fully-formed and isolated bodies, especially in dense stellar environs. Several types of dissipative effects may bind two lone stars together, including dynamical friction in a gaseous medium (Rozner et al. 2023), tidal heating of one star by another ('tidal capture'; e.g., Fabian et al. 1975; Generozov et al. 2018), and gravitational wave emission in a close passage of two compact objects ('gravitataional wave capture'; e.g., Quinlan & Shapiro 1989). In this work, we explore a purely Newtonian phenomenon, three-body binary formation (3BBF), in which three isolated (energetically unbound) bodies pass near each other and gravitationally scatter to form a new binary. The leftover single acts as a source of dissipation in this scenario, a catalyst, transferring gravitational potential energy into the kinetic energies of the single and a new binary's center-of-mass.

The body of work investigating 3BBF is presently very limited compared to investigations of the aforementioned binary formation mechanisms. The historical lack of interest is likely due to over-generalization of early analytic estimates of 3BBF's impact on star clusters (Heggie 1975; Stodolkiewicz 1986; Goodman & Hut 1993). The usual narrative states that the 3BBF rate is negligible over most of a cluster's dynamical lifetime, except in the short window of time central densities spike during the core collapse process (e.g., Hut 1985; Freitag & Benz 2001; Joshi et al. 2001) or even there-

after (e.g., Statler et al. 1987; Hut et al. 1992).[1] Such studies generally predate the cluster modeling community's widespread incorporation of primordial binaries and realistic IMFs—and therefore neglect essential BH dynamics. Due to the 3BBF rate's steep mass dependence in its classic $\sim n^3 G^5 m^5/\sigma^9$ scaling (e.g., Heggie 1975; Kulkarni et al. 1993; O'Leary et al. 2006; Banerjee et al. 2010; Morscher et al. 2013, 2015), BH populations greatly enhance 3BBF. Without such massive bodies, efficient 3BBF would require an extreme cluster density only achieved in very deep core collapse beyond the central density of today's *observationally* 'core-collapsed' Milky Way globular clusters, whose cores remain supported by central binary burning (Weatherford et al. 2023). In fact, accounting for BH retention and using the 3BBF recipe of Morscher et al. (2015), Weatherford et al. (2023) predict that 3BBF occurs frequently in globular clusters—an overwhelming majority involving BHs—and cumulatively powers many high-speed ejections. Due to its impact on the formation of dynamically active BH binaries and high-speed ejection, 3BBF is essential for understanding star cluster evolution, BH mergers, and high-velocity stellar populations.

Earlier disinterest in 3BBF may also stem from its overwhelming tendency to form soft binaries, coupled with the assumption that such binaries are unlikely to survive long enough to contribute significantly to cluster dynamics via binary burning. Indeed, strong encounters quickly disrupt most soft binaries and also tighten those formed especially hard until they merge or are ejected from the cluster (e.g., Hut & Inagaki 1985; McMillan 1986; Goodman & Hernquist 1991; Bacon et al. 1996; Chernoff & Huang 1996; Fregeau et al. 2004a). This reasoning was previously used to justify neglecting 3BBF, either entirely (e.g., Joshi et al. 2000; Fregeau et al. 2003), or if none of the bodies were BHs (e.g., Morscher et al. 2015), in prescription-based Monte Carlo star cluster models such as `CMC` (Rodriguez et al. 2022). Unfortunately, this neglects the formation of binaries of only moderate hardness, with or without BHs. A staggering result of Goodman & Hut (1993) is that soft binaries from 3BBF, though typically short-lived, form so frequently that the small fraction which *do* survive and harden sufficiently may yield over 90% of hard binaries over long timescales in massive star clusters. These binaries would, in fact, survive long enough to contribute substantially to binary burning but are not typically accounted for in cluster modeling (outside of direct N-body simulations, which have their own limitations; see below).

Despite renewed interest, modern 3BBF recipes (e.g., Goodman & Hut 1993; Ivanova et al. 2005, 2010; Morscher et al. 2013, 2015) are untested by numerical scattering experiments. The only two examples of such studies, Agekyan & Anosova (1971) and Aarseth & Heggie (1976)—hereafter referenced as AH76—suffered from small sample sizes and were limited to equal point masses. And while full direct N-body codes capture 3BBF naturally, a detailed analysis of this physical process is challenging due to the rarity of the event in the low-mass, small-N, or low-density clusters typically modeled by such codes (Tanikawa et al. 2013; Marín Pina & Gieles 2023).

To this day, the direct N-body approach borders on being too computationally expensive to practically simulate globular clusters that are simultaneously as massive, old, *and* dense as those in the Milky Way (Wang et al. 2016; Arca Sedda et al. 2023). Conversely, much faster Monte Carlo and semi-analytic codes use highly approximate recipes (e.g., Rodriguez et al. 2022, and references therein) for 3BBF rather than direct integration with a small-N-body code—e.g., FEWBODY (Fregeau et al. 2004a) or TSUNAMI (Trani & Spera 2023). In fact, the prescription in `CMC` automatically pairs the two most massive bodies in three-body "interactions" at a numerically untested rate based on the local stellar density, velocities, and masses. No rigorous justification exists for this pairing, yet it may have dramatic implications for newly formed binaries and cluster evolution.

Here, we present a rigorous framework for 3UB interactions and self-consistently investigate 3BBF physics through direct N-body scattering experiments. Our methodology builds upon the work done by AH76 with adjustments made to correct a minor inconsistency in the Monte Carlo sampling scheme AH76 adopted from Agekyan & Anosova (1971). Our investigation is built on the TSUNAMI integrator (Trani & Spera 2023; Trani, Spera, & Atallah 2024, in preparation) and the CUSP-BUILDING Python package (Atallah et al. 2023).

Our methodology is detailed in Section 2, explaining the initial condition algorithm in Section 2.1. We reproduce the results of AH76 using their 3UB algorithm in Section 2.2 and also justify the need for correcting the original AH76 algorithm by analyzing a simple "particle-in-box" simulation. Section 2.3 features a first-principles derivation of the 3UB encounter rate complementary to our algorithm, validated to be correct to within percent error in the particle-in-box sim-

[1] Here, "core collapse" is the process by which the most massive objects in a stellar cluster rapidly evacuate kinetic energy from central regions, sink deeper into the cluster (dynamical friction), and subsequently contract the core to increasingly higher densities, a process that is halted by 3BBF.

ulation. In Section 3, we broadly explore 3BBF in the point mass limit. The equal-mass hard binary formation rate predicted by Goodman & Hut (1993) is reproduced in Section 3.1.2 and we discuss our findings regarding super-thermal wide binary formation in Section 3.1.3. We investigate the 3UB scattering of unequal point masses in Section 3.2 before applying our framework to the scattering of bodies with finite-size, main-sequence (MS) stars and black holes (BHs) in Section 4. We lay out our conclusions and discuss next steps in Section 5.

2. METHODS

Our three-body scattering experiments are conducted with the CUSPBUILDING Python package (Atallah et al. 2023), a Monte Carlo scattering framework built upon the TSUNAMI integrator (Trani & Spera 2023; Trani, Spera, & Atallah 2024, in preparation). TSUNAMI is a direct N-body integrator based on Mikkola's algorithmic regularization (Trani & Spera 2022; Trani et al. 2019a,b), using the leapfrog algorithm in conjunction with Bulirsch-Stoer extrapolation (Stoer & Bulirsch 1980) and the chain-coordinate system introduced in Mikkola & Aarseth (1993).

These techniques allow TSUNAMI to follow close encounters with extreme accuracy without reducing the integration time-step, unlike traditional integrators (e.g., Fregeau et al. 2004b). This makes TSUNAMI an ideal code for integrating any compact few-body system, including extreme mass-ratio configurations, such as stellar-mass binary BH scattering in the vicinity of an SMBH (Trani et al. 2023). The TSUNAMI/CUSPBUILDING framework yields extreme precision and speed, with a typical evaluation rate of ∼200 3UB scatterings per second, per CPU core. In total, we generate over 10^{10} 3UB encounters, one of the largest sets of scattering interactions yet generated for a single work.

As in Agekyan & Anosova (1971) and AH76, we initiate all bodies relative to the origin of an inertial reference frame, O. This origin serves as the "target" of all three bodies. Unlike in AH76, we adopt a "spherical" initial condition sampling method in contrast to their "cylindrical" method; we elaborate on this distinction and provide a robust numerical justification for adjusting this algorithm in Sections 2.1 and 2.2.

2.1. *Initial Condition Algorithm*

The initial condition algorithm may be subdivided into three parts:

1. Select the masses and velocity vectors of the three scattering bodies.

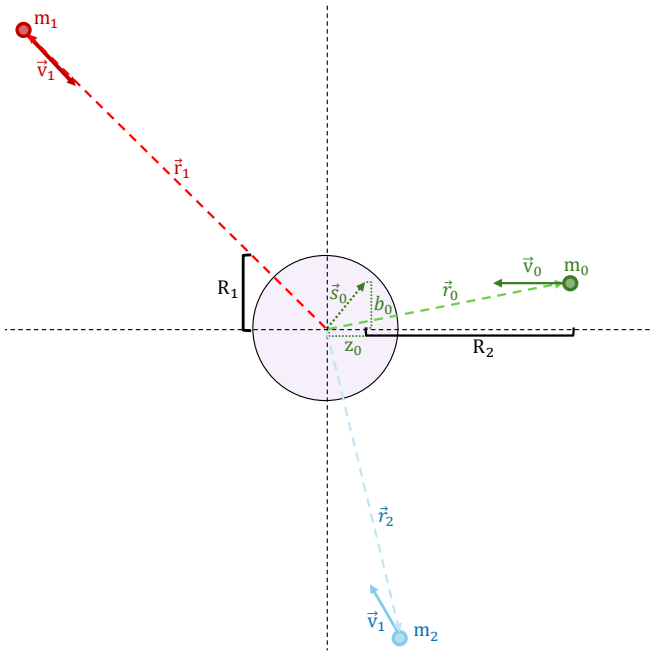

Figure 1. A schematic of our three unbound body (3UB) initial condition algorithm, projected in 2D. The labels used here are in line with the prescriptions of Equations (1)–(5).

2. Randomly assign a point in a sphere of radius R_1 to each body. This point is drawn from a distribution explicitly uniform in the volume of a sphere.

3. Pull each body backward in time along a straight line using their individual velocity vectors. This procedure approximates gravitationally isolating the three bodies far from the region of interaction.

We begin by defining a set of initial properties for each body: initial masses, $m_{\rm i}$, and velocities, $\vec{v}_{\rm i}$, with ${\rm i} = \{0, 1, 2\}$. Relative to the origin, a set of impact parameters $b_{\rm i}$ and offsets $z_{\rm i}$ (along the line parallel to the body's velocity) are then sampled using the following relations:

$$\begin{aligned} b_{\rm i} &= s_{\rm i} \sin\phi_{\rm i} \\ z_{\rm i} &= s_{\rm i} \cos\phi_{\rm i} \\ s_{\rm i} &= \sqrt[3]{\mathcal{U}_{\rm i}(0,1)}\, R_1 \\ \phi_{\rm i} &= \cos^{-1}\left[\mathcal{U}_{\rm i}(-1,1)\right] \\ R_1 &= 2\chi_1 b_{90} \\ b_{90} &= \max\left[\frac{G(m_{\rm i}+m_{\rm j})}{\langle(\vec{v}_{\rm i}-\vec{v}_{\rm j})^2\rangle}\right]. \end{aligned} \tag{1}$$

Here, R_1 is the radius of an "interaction volume" centered on O, χ_1 scales R_1 to probe strong and weak encounter regimes, b_{90} is the largest average 90° deflection impact parameter of all two-body combinations, $\phi_{\rm i}$ is an inclination angle drawn from an inclination distribu-

tion uniform in cosine, and $\mathcal{U}_{\rm i}(0,1)$ is a random number sampled uniformly between 0 and 1. This procedure is equivalent to sampling points within a sphere of radius R_1 from a distribution uniform in volume.[2] The drawn points are expressed in vector notation as

$$\vec{s}_{\rm i} = b_{\rm i}\vec{e}_{\rm i}^{\,\perp} - z_{\rm i}\vec{e}_{\rm i}^{\,\parallel} \tag{2}$$

with $\vec{e}_{\rm i}^{\,\perp}, \vec{e}_{\rm i}^{\,\parallel}$ representing basis vectors perpendicular and parallel, respectively, to the randomly sampled velocity vectors of each body.

The set of points sampled by the above procedure are not the actual initial conditions for the scattering experiment. Rather, they describe a point in time—the *epoch time*—at which all three bodies, if they were to travel on straight-line trajectories, would all be located simultaneously within the interaction volume of radius R_1. To initialize the scattering experiment with the bodies far away from the interaction volume, we then pull each body backwards in time along the straight line parallel to its velocity vector, effectively applying an offset in each body's arrival time to the interaction region. If the bodies were to travel on straight-line trajectories, such initial conditions would therefore *guarantee* that all three bodies are in the interaction volume at the epoch time. In reality, the trajectories will curve due to gravitational focusing, but the mathematical chaos of the three-body problem prevents the construction of a general, unbiased, and analytically-sampled choice of initial conditions that would make the same guarantee while accounting for the influence of gravity.

To pull each body backwards in time, we need to select an appropriate time-offset. Following from AH76, we begin by selecting a reference distance, R_2. By dividing R_2 by the velocity magnitude of the slowest moving body, we obtain the epoch time, $t_{\rm e}$:

$$\begin{aligned} R_2 &= 2\chi_2 b_{90} \\ t_{\rm e} &= \frac{R_2}{\min(v_{\rm i})}, \end{aligned} \tag{3}$$

where χ_2 is a scaling parameter modulating R_2; as in AH76, we set $\chi_2 = 15\chi_1$. The offset distance, drawn backward along the aforementioned straight-line trajectory, is therefore

$$\Delta\vec{r}_{\rm i}^{\,\parallel} = -\vec{v}_{\rm i}t_{\rm e} = -v_{\rm i}t_{\rm e}\vec{e}_{\rm i}^{\,\parallel}. \tag{4}$$

[2] To the contrary, AH76 explores the parameter space using the volumes of arbitrarily rotated, overlapping cylinders—setting $b_{\rm i} = \sqrt{\mathcal{U}_{\rm i}(0,1)}\,R_1$ and $z_{\rm i} = \mathcal{U}_{\rm i}(-1,1)\,R_1$.

With these offsets in hand, the initial conditions for each body are then

$$\begin{aligned} \vec{r}_{\rm i} &= b_{\rm i}\vec{e}_{\rm i}^{\,\perp} - (z_{\rm i} + v_{\rm i}t_{\rm e})\vec{e}_{\rm i}^{\,\parallel}, \\ \vec{v}_{\rm i} &= v_{\rm i}\vec{e}_{\rm i}^{\,\parallel}. \end{aligned} \tag{5}$$

Finally, the initial orientations/basis vectors of each body are rotated along standard, randomly drawn Euler angles (i.e., $\Omega_0\Omega_1\Omega_2$) relative to O. We redraw both the locations $\vec{s}_{\rm i}$ of the bodies at $t_{\rm e}$ and the Euler rotations if any two-body combination or the net three-body system have a negative total energy in the two- or three-body center-of-mass frames, respectively. Just as in AH76, we do not filter out 3BBF event/strong encounter occurring outside of the fixed interaction volume. An example schematic of a 3UB initial condition is displayed in Figure 1.

The duration of every simulation is entirely adaptive and individualized to each scattering initial condition. CuspBuilding integrates the system until $t = 2t_{\rm e}$ before assessing whether all outgoing hierarchies are "energetically isolated." A hierarchy is energetically isolated if the gravitational potential energy between each hierarchy is less than 1% of their relative kinetic energy. Here, a single body system is still a hierarchy of rank 1. If all hierarchies are isolated, then CuspBuilding considers the system to have reached its final state and terminates integration.

2.2. *Replicating & Assessing Aarseth & Heggie 1976*

Before exploring new results, it is useful to reproduce the original 3BBF investigation conducted by Aarseth & Heggie (1976), using their unmodified algorithm (i.e., with a cylindrically-sampled impact parameter) in the Newtonian, point mass regime. Figure 2 compares the 3BBF probability—the fraction of 3UB scattering experiments resulting in a binary forming—as a function of χ_1, between AH76 and our Tsunami re-implementation of their method. As seen in the lower panel, our re-implementation results in no more than ±20% difference in the 3BBF probability from AH76, easily explained by the dramatic increase in sample size and computing resources. We also recover the χ_1^{-2} dependency in the total 3BBF probability and validate that the AH76 algorithm correctly results in indistinguishable bodies (with

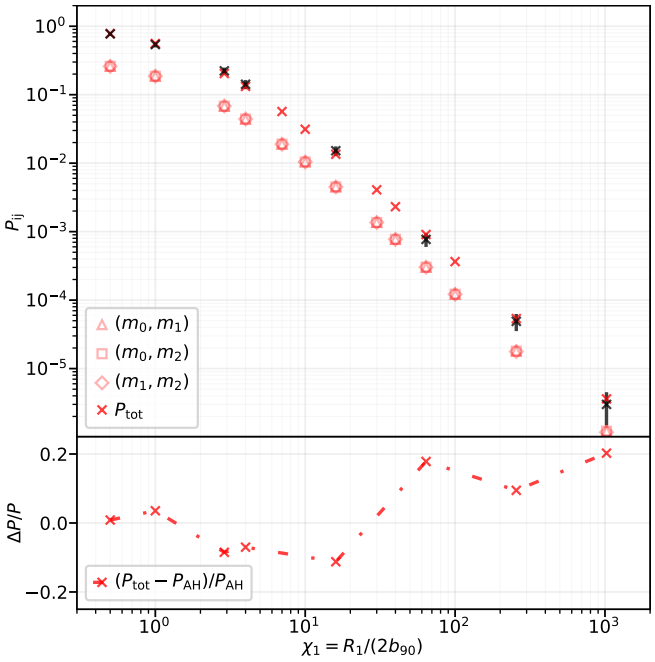

Figure 2. Reproduction of three-body binary formation (3BBF) probabilities reported in Aarseth & Heggie (1976). *Top Panel*: Probability P_{ij} of forming a binary containing bodies i and j as a function of dimensionless impact parameter χ_1 (see Equation 1) through the interaction of three equal-mass bodies initially on unbound trajectories. The initial velocities at infinity are drawn from a Maxwellian distribution. Red crosses mark the total 3BBF probability, independent of pairing, while shapes represent the pair-specific probabilities. As expected, equal-mass bodies have equal probabilities of pairing. Black crosses, with error bars, are the values reported in AH76. *Bottom Panel*: Fractional difference in probabilities between our results and AH76. We see good agreement ($\Delta \lesssim 20\%$).

identical mass and velocity) having equal likelihood of pairing; see the red shapes in the top panel.[3]

Unfortunately, the initial condition algorithm employed by AH76 probes an asymmetric encounter volume comprised of randomly oriented overlapping cylinders, expanding the effective encounter volume by $50\% - 150\%$ when compared to our desired spherical sampling algorithm. Fewer binaries form as a result (see Section 3.1) and those that do are softer. To test whether our algorithm is self-consistent with an isotropic assumption, as was intended in AH76, we generated a simple "particle-in-box" simulation of non-interacting point masses with periodic boundary conditions. A number of standard assumptions were correctly validated here: (i) The classic geometric encounter rate, $\langle \Gamma \rangle = \pi n r^2 v$, was found correct to within percent error. (ii) Our newly derived encounter rate, Γ^{3B}, (see Section 2.3) is found to be correct to within small number fluctuations. (iii) The radial distribution of three bodies occupying a fixed, spherical volume at random times in the simulation scales as r_i^3/R_1^3, where r_i is the radial location of the body passing through the fixed volume of radius R_1.

[3] We also note we have rigorously tested many other 3UB configurations, such as targeting an incoming single at the center-of-mass of a hyperbolic two-body encounter, the setup often used in analytic estimates of the 3BBF rate. We found that even for the case of equal masses and velocities, such setups always bias the pairing probability toward the incoming single.

2.3. *Encounter Rate*

We present the first *encounter rate* that correctly predicts the probability per unit time of a 3UB interaction occurring. Note that an encounter rate is not a formation rate; the formation rate may be determined by calculating a numerically determined efficiency through many scattering interactions. Previous work (Heggie 1975; Goodman & Hut 1993) assessed 3BBF using detailed balance, bypassing the need for an encounter rate and directly predicting a formation rate.

We consider two different geometric interpretations for the encounter rate:

- A stationary spherical volume embedded in a host environment containing particle fields with local number densities n_i and velocity dispersions σ_i for each of up to three distinct populations $i \in [1, 3]$.
- A spherical volume containing one target body—not necessarily at its center—that moves with the velocity of the target and thus has the same velocity dispersion, σ_t, relative to its host environment.

To derive the encounter rate, we first define the probability of finding a body within an enclosing volume embedded in a particle field,

$$P_i = n_i V_i, \tag{6}$$

where V is the enclosing volume and $n_i V_i \ll 1$. The encounter rate is thus

$$\Gamma_i = \frac{dP_i}{dt} = n_i \frac{dV_i}{dt}, \tag{7}$$

where dV/dt is the volumetric flow-rate. Fundamentally, the one-dimensional flow-rate through a volume may be expressed as

$$\frac{dV_i}{dt} = \frac{dV_i}{dz_i}\frac{dz_i}{dt} = A_i v_i \tag{8}$$

where A_i is the projected cross-sectional area in the flow direction of a particle field, and v_i is the velocity of that

fluid. If $P_{\rm i}$ is labeled as an "event", then the probability of three independent and simultaneous events, a 3UB event, is

$$\begin{aligned} P_{\rm 3B} &= \frac{1}{l!} P_{\rm i} P_{\rm j} P_{\rm k} \\ &= \frac{n_{\rm i} n_{\rm j} n_{\rm k}}{l!} V_{\rm i} V_{\rm j} V_{\rm k}, \end{aligned} \tag{9}$$

where $l!$ is the standard correction for joint Poisson distributions when particles are drawn from the same field (e.g., $l = 2$ if two particles are selected from the same field). The respective mean encounter rate is

$$\Gamma_{\rm 3B} \equiv \frac{n_{\rm i} n_{\rm j} n_{\rm k}}{l!} \left(v_{\rm i} A_{\rm i} V_{\rm j} V_{\rm k} + v_{\rm j} A_{\rm j} V_{\rm i} V_{\rm k} + v_{\rm k} A_{\rm k} V_{\rm i} V_{\rm j} \right). \tag{10}$$

For all bodies to meet within the same sphere of radius R_1, we may set $V_{\{\rm i,j,k\}} = 4\pi R_1^3/3$ and $A_{\{\rm i,j,k\}} = \pi R_1^2$. The mean encounter rate then becomes

$$\Gamma_{\rm 3B} = \frac{3\beta^3}{4\, l!} R_1^8 n_{\rm i} n_{\rm j} n_{\rm k} (v_{\rm i} + v_{\rm j} + v_{\rm k}), \tag{11}$$

where $\beta \equiv \frac{4\pi}{3}$, and the rate per unit volume is

$$\tilde{\Gamma}_{\rm 3B} \equiv \frac{\Gamma_{\rm 3B}}{V} = \frac{3\beta^2}{4\, l!} R_1^5 n_{\rm i} n_{\rm j} n_{\rm k} \left(v_{\rm i} + v_{\rm j} + v_{\rm k} \right). \tag{12}$$

For the case of an isotropic Maxwellian velocity distribution in each particle field, then

$$\tilde{\Gamma}_{\rm 3B} = \frac{3\beta^2}{\sqrt{2\pi}\, l!} R_1^5 n_{\rm i} n_{\rm j} n_{\rm k} \left(\sigma_{\rm i} + \sigma_{\rm j} + \sigma_{\rm k} \right), \tag{13}$$

where $\sigma_{\rm i}$ is the velocity dispersion of each particle species. This rate assumes a small enough volume that the number density of the local field is roughly constant.

To find an encounter rate relative to an individual target already embedded within a spherical volume of radius R_1 (i.e., the "per-body" rate), we may set $P_{\rm k} = 1$. Here, $P_{\rm 3B} = \frac{1}{l!} P_{\rm i} P_{\rm j}$. Following the above calculation, the three-body encounter rate per body is then

$$\Gamma_{\rm 3B,pb} = \frac{3\beta^2}{4\, l!} R_1^5 n_{\rm i} n_{\rm j} \left(v_{\rm i}^{\rm rel} + v_{\rm j}^{\rm rel} \right), \tag{14}$$

where $v_{\rm i}^{\rm rel}$ is the velocity of body i relative to the target, body k. For a Maxwellian velocity distribution,

$$\begin{aligned} \Gamma_{\rm 3B,pb} &= \frac{3\beta^2}{\sqrt{2\pi}\, l!} R_1^5 n_{\rm i} n_{\rm j} \left(\sigma_{\rm i}^{\rm rel} + \sigma_{\rm j}^{\rm rel} \right) \\ \sigma_{\rm i}^{\rm rel} &= \sqrt{\sigma_{\rm t}^2 + \sigma_{\rm i}^2}, \end{aligned} \tag{15}$$

where $\sigma_{\rm t}$ is the velocity dispersion describing the motion of the target body. This per-body encounter rate and the volumetric rate are correct to within percent-level in our simple particle-in-box simulation (Figure 3), generated with non-interacting particles and periodic boundary conditions.

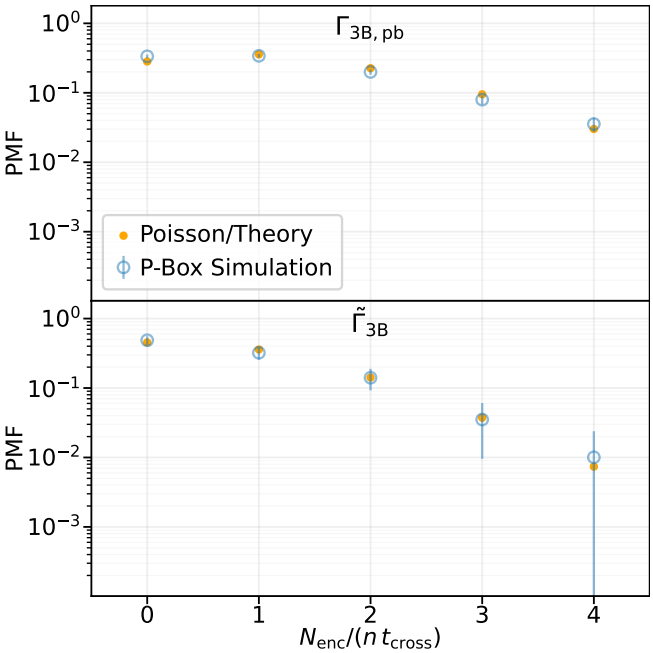

Figure 3. Yellow points show the discrete probability density function (PMF) for the number of times ($N_{\rm enc}$) three particles in a particle-in-box simulation are simultaneously within a small spherical volume at the box's center. The count on the horizontal axis is expressed as a rate by dividing $N_{\rm enc}$ by a large multiple, n, of the box's average crossing time, $t_{\rm cross}$, given particle speeds sampled from a Maxwellian distribution. The upper and lower panels show the per-body and volumetric encounter rates, with $n = 5$ and $n = 50$, respectively. Each particle travels at constant speed and elastically bounces off the walls of the box. The count $N_{\rm enc}$ increases by one each time a particle passes into the encounter volume while at least two other bodies are already inside the volume (or one other body in the per-body rate). The simulation results are compared to our derived encounter rates from Equation (13)—blue points—by sampling from a Poisson distribution, $P(N) = (\tilde{\Gamma}_{\rm 3B}\, \delta t)^N e^{-\tilde{\Gamma}_{\rm 3B}\, \delta t}/N!$, where $\delta t = n\, t_{\rm cross}$.

Finally, note that if all three particle fields are described by the same masses and local velocity dispersion, then substituting Equation (1) into Equation (12) results in the scaling

$$\tilde{\Gamma}_{\rm 3B} \propto \chi_1^5 \frac{G^5 m^5 n^3}{\sigma^9}. \tag{16}$$

This reproduces the classic $\sim G^5 m^5 n^3 \sigma^{-9}$ scaling from earlier estimations of the three-body encounter rate (e.g., Goodman & Hut 1993; Heggie & Hut 2003; Binney & Tremaine 2008). However, not all three-body encoun-

ters result in formation of a binary. The true volumetric 3BBF rate $\tilde{\Gamma}_{\rm F}$ must therefore be numerically determined and satisfies the relation

$$\tilde{\Gamma}_{\rm F} = P_{\rm ij}\tilde{\Gamma}_{\rm 3B}, \tag{17}$$

where $P_{\rm ij}$ is the numerically determined probability of forming a binary (with pairing $\{i, j\}$) per 'encounter' occurring at rate $\Gamma_{\rm 3B}$.

3. 3BBF IN THE POINT MASS LIMIT

We now explore the outcomes of 3UB scatterings for point-particles of both equal and unequal masses. To be consistent with our validated encounter rate, derived by invoking spherical symmetry, we use our corrected algorithm that probes time offsets spherically (Section 2.1) instead of using the cylindrical prescription of AH76.

To aid astrophysical interpretation of our results, we first define our criteria for "hard" and "soft" binaries. Traditionally, this refers to binaries with binding energies greater than (hard) or less than (soft) the typical kinetic energy of gravitating bodies in the local environment (Heggie & Hut 2003; Binney & Tremaine 2008). We make a slight modification by using the "fast" and "slow" criteria justified by Hills (1990), where the hardness of a newly formed binary is determined instead by its orbital velocity relative to the local velocity distribution surrounding the 3UB encounter. The "fast/slow" boundary is

$$a_{\rm fs,ij} = \frac{G(m_{\rm i} + m_{\rm j})}{\langle v_{\rm rel}^2 \rangle}, \tag{18}$$

where $m_{\rm i}, m_{\rm j}$ are the masses of the two newly paired bodies and $\langle v_{\rm rel}^2 \rangle$ is the typical mean-squared relative velocity of the new binary, simplified to be $\langle v_{\rm rel}^2 \rangle = 3\sigma_{\rm rel}^2 = 6\sigma^2$ for an isotropic gas described by a Maxwellian with a 1D velocity dispersion σ. Note that $\max(a_{\rm fs,ij}) = b_{90}$.

The definition of $a_{\rm fs,ij}$ and b_{90} are dependent on the velocity dispersion selected for a set of scattering experiments. In effect, we may extract "scale-free" results in the Newtonian regime by simply dividing length scales by b_{90}, $a_{\rm fs,ij}$, or R_1, hence why we frequently employ χ_1 as an independent variable in all of our experiments. When we refer to "hard" and "semi-soft" binaries, we mean binaries with $a_{\rm ij} < a_{\rm fs,ij}$ and $a_{\rm ij} < 10\, a_{\rm fs,ij}$, respectively. Semi-soft binaries include hard binaries, though their contribution is negligible since the binary 3BBF probability decreases steeply with binary hardness.

Note that, throughout the entirety of our results, we find no evidence of any 3UB encounter or 3BBF event exhibiting resonant behavior in any regime. Here, resonance is the process by which a temporary bound state forms containing *all* of the scattering bodies, usually characterized by a long, chaotic orbital dance. CUSP-BUILDING provides output when encounters are long-lived (e.g., the encounter is unresolved at $t > 2t_{\rm e}$) and none of our scattering experiments triggered this condition. Additionally, every single animation of 3BBF encounters we have produced in every regime (e.g., hard, soft, unequal-mass, etc.) are distinctively perturbative encounters, characterized by up to two slingshots shared by the three interacting bodies. Resonant interactions have long been understood to be strongly disfavored, if not impossible, when the total energy in the center-of-mass frame of the three-body system is positive (Heggie & Hut 2003; Binney & Tremaine 2008).

3.1. *Equal Point Masses*

In Figure 4, we show the 3BBF probability for the case of equal point masses as a function of the dimensionless impact parameter χ_1. Colors distinguish binaries formed of different hardness while the point styles compare the outcome using the cylindrical AH76 algorithm (crosses) versus our spherical correction to their algorithm (points). Spherical sampling boosts the 3BBF probability at all scales by $\sim$10% − 50% when compared to AH76's cylindrical sampling method. For both sampling methods, the 3BBF probability for binaries with $a_{\rm ij} < R_1$ and $\chi_1 \gg 1$ scales as $P_{\rm ij} \propto \chi_1^{-4.5}$. This is slightly shallower than the χ_1^{-5} scaling one would expect from equating the 3BBF rate to the 3UB encounter rate (e.g., Goodman & Hut 1993; Ivanova et al. 2005, 2010; Binney & Tremaine 2008; Morscher et al. 2013, 2015).

Binaries from 3BBF also exhibit several nearly geometrically scale-free properties when scaled to R_1. In the center panel of Figure 5, we show the cumulative distribution for binary semi-major axes (SMA) from 3BBF, normalized by the radius of the interaction volume, R_1. In the bottom panel, we display the eccentricity distribution of binaries with $a > R_1$—which we will periodically reference as *wide binaries*—and binaries with $a < R_1$. In both panels, the color of the distribution denotes the value of χ_1 used in the scattering experiment. We find that both the SMA and eccentricity distributions do not depend on χ_1 in that they are nearly independent of the size of the interaction volume (geometrically scale-free). Specifically, the binaries with $a < R_1$ are well-described by the thermal eccentricity distribution (dashed black; $f(e) = 2e$, $C(e) = e^2$) while binaries overall (dominated by those with $a > R_1$) have super-thermal eccentricity.

It may appear counter-intuitive that 85% of the binaries have an SMA larger than the radius of the interaction volume, $a > R_1$, and super-thermal eccentricities. However, there is no lower limit on binding energy, and so there is no upper bound on SMA. Separately, the di-

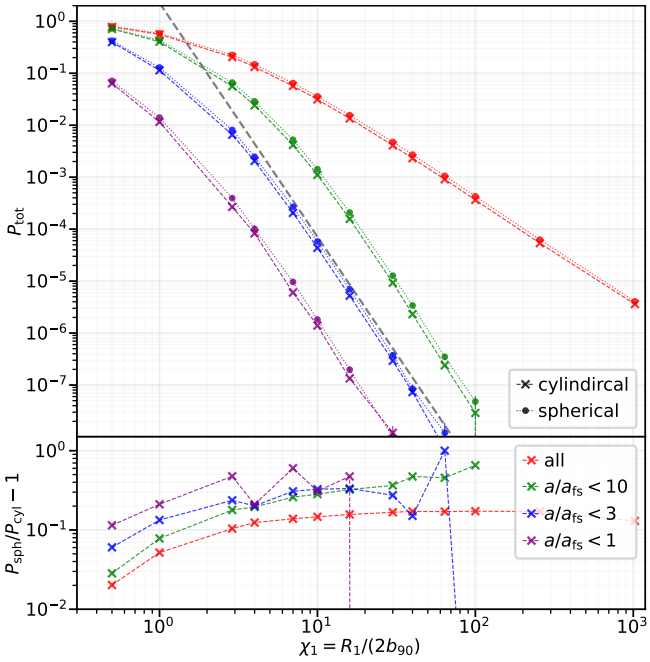

Figure 4. Equal-mass 3BBF probabilities colored by minimum hardness with comparisons between the spherical and cylindrical (AH76) initial condition algorithms. *Top Panel*: 3BBF probability, $P_{\rm ij}$, versus dimensionless impact parameter, χ_1; all bodies are drawn from an identical Maxwellian velocity distribution. The 95% confidence intervals are included as error bars for all points under the assumption 3BBF is a Poissonian process. However, these error bars are difficult to see for any probability $\gtrsim 10^{-7}$ due to the large sample size (10^9 scatterings per value of χ_1). As expected, $P_{\rm ij} \propto \chi_1^{-2}$ in the "soft-binary" limit (large χ_1), in accordance with the scaling identified by AH76. Both algorithms produce a $P_{\rm ij} \propto \chi_1^{-4.5}$ decay for binaries with $a_{\rm ij} \lesssim R_1$ (the fit is the gray dashed line), as opposed to the χ_1^{-5} decay expected from standard analytic estimates; the discrepancy is likely due to the complicated nature of gravitational focusing in 3UB (see text). *Bottom Panel*: Scatter plot quantifying the difference in probability between the two algorithms. We find that the harder the binary formed the greater the boost spherical sampling provides to 3BBF, up to ∼30% for hard binaries (purple).

ameter of the smallest sphere containing all three bodies at any point during integration, $d_{\rm min}$, sets the maximum periapse, $a(1-e) < d_{\rm min}$, in all 3BBF and the minimum apoapsis, $a(1+e) > d_{\rm min}$, in > 99% of 3BBF, independent of algorithm and binary hardness (Figure 6). For low binding energies (large SMA), $a \gg R_1$, implying that the resultant eccentricity distribution must be super-thermal ($\langle e \rangle \sim 1$) to satisfy the inequality.

Our results unambiguously confirm that binaries with with $a < R_1$, encompassing all hard binaries, are born with thermal eccentricities. This is a classic prediction for both hard and soft binaries under the assumption

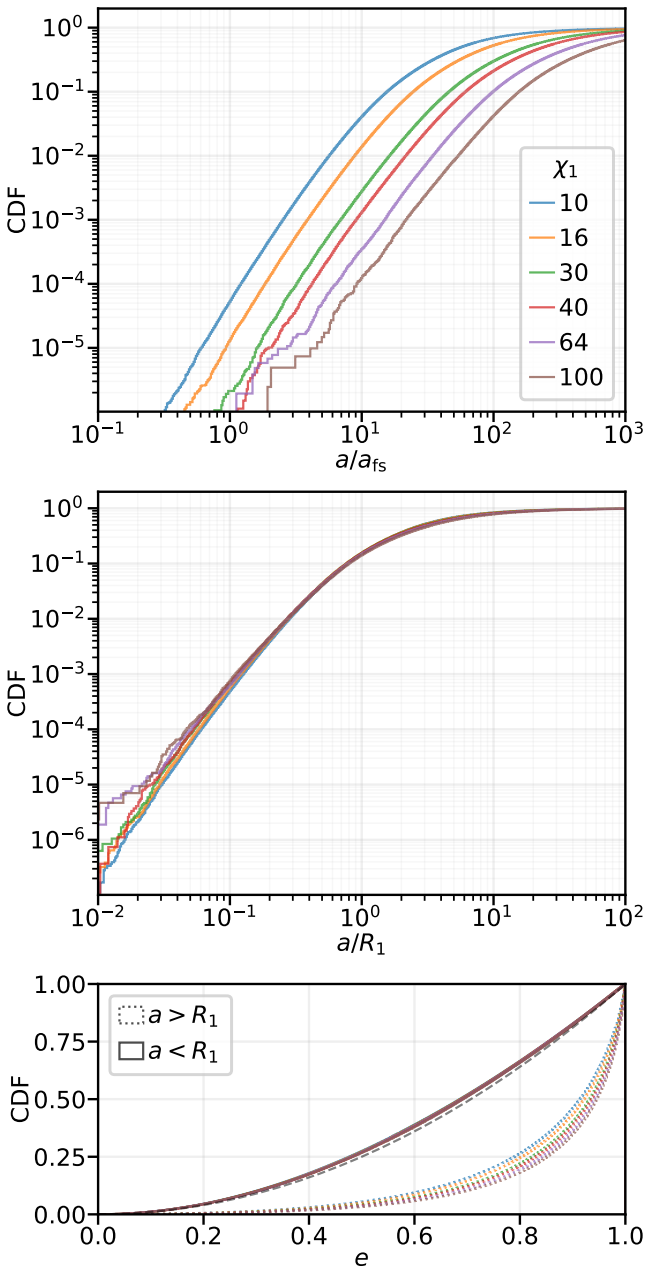

Figure 5. *Top Panel*: CDF of binary semi-major axis a normalized by the fast-slow boundary $a_{\rm fs}$ during equal point mass 3BBF. Each curve represents an experiment with a different value of $\chi_1 = R_1/(2b_{90})$. *Middle Panel*: Identical to top panel, except the CDF is normalized instead by the radius of the encounter volume, R_1. Binaries formed with $a \lesssim R_1$ account for ≈15% of pairings. Independent of χ_1, the cumulative semi-major axis distribution scales approximately as $C(a) \sim a^3$. *Bottom Panel*: The corresponding CDFs for binary eccentricity e. Irrespective of χ_1, the e distribution for binaries with $a < R_1$ (overlapping solid curves) is nearly thermal, $C(e) \approx e^2$, while the e distribution including all binaries (overwhelmingly soft binaries; dashed curves) is super-thermal, $C(e) \approx e^\beta$ for $\beta > 2$. So the widest binaries formed via 3BBF tend to have super-thermal eccentricity.

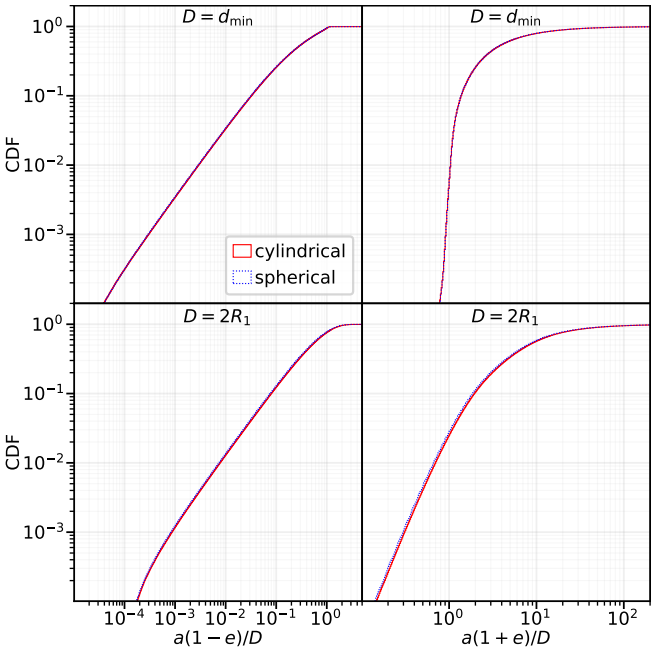

Figure 6. CDFs of pericenter and apocenter distances normalized by (*top*) the diameter $d_{\rm min}$ of the smallest sphere containing all three bodies at any time during the 3BBF interaction and (*bottom*) the diameter of the interaction volume, $2R_1$. These CDFs include every binary in the equal-point-mass scattering experiments with $\chi_1 = 10$. Colors highlight the algorithm employed, the original cylindrical algorithm (solid red) from AH76 versus our corrective spherical algorithm (dotted blue). In both cases, the minimum apoapse and maximum periapse distances are very nearly $d_{\rm min}$. This shows that $d_{\rm min}$ dictates the binary's orbital elements and implies that the fundamental physics of 3BBF is independent of the initial condition algorithm, so long as $\chi_2 > \chi_1 \gg 1$.

they have undergone many successive encounters within their environment (Jeans 1919; Heggie 1975). Sample 3UB trajectories resulting in hard and wide 3BBF, as well as in no 3BBF (a simple flyby of three single bodies), are displayed in Figure 7. The figure shows that 3BBF occurs as a single, non-resonant event, implying that the thermal distributions may be more fundamental to binary formation than previously assumed, independent of gravothermal equilibrium, detailed balance, or any need for many successive encounters.

3.1.1. *Choice of* χ_1

Having examined how the 3BBF probability depends on χ_1 in the case of equal point masses, it is natural to wonder what is a proper choice of χ_1. Setting χ_1 high enough that R_1 exceeds the interparticle distance in the host environment would clearly violate the assumed isolation of the interaction from its surroundings. Yet simply anchoring R_1 to the interparticle distance is not computationally optimal; since the 3BBF probability drops steeply with increasing χ_1, choosing too large a χ_1 needlessly inflates the number of scattering experiments required to achieve a robust sample of binaries. However, χ_1 cannot be made arbitrarily small without biasing the properties of the binaries that are formed.

In the limit $\chi_1 \to 0$, the initial positions and velocities of all bodies are focused toward a point because $R_2 = 15R_1$ ($\chi_2 = 15\chi_1$) in the AH76 method. This minimizes the angular momentum in the global reference frame and causes the 3BBF probability to saturate (no longer follow a simple power law scaling with χ_1). By initializing the bodies deeper within their mutual potential wells, this limit also results in a total initial energy much nearer to zero than in a scattering experiment conducted at higher χ_1. Since the 3UB problem requires total positive energy, shrinking χ_1 too far would bias the initial conditions to be just barely unbound. From an algorithmic perspective, the vast majority of randomly-generated initial conditions in this limit would sample at least two bound bodies, and have to be thrown out. This artificially truncates the energy–angular momentum parameter space that would otherwise be obtained naturally from the isotropically sampled Maxwellian velocity distributions.

A key limiting factor in choosing χ_1 and χ_2 is the average interparticle distance, $\langle r \rangle$, of the local environment the bodies live in. Specifically, to satisfy the assumption of an isolated 3UB encounter, then R_1 must be $< \langle r \rangle$. We can form a qualitative picture by first writing $\langle r \rangle$ in terms of fundamental quantities of the Plummer model,

$$\langle r \rangle = \frac{GM_{\rm P}}{6} \frac{\sigma_{\rm c}^{4/3}}{\sigma^{10/3}} N^{-1/3}, \tag{19}$$

where $M_{\rm P}$ is the total mass of the Plummer cluster, $\sigma_{\rm c} = \sqrt{\frac{GM}{6\,b_{\rm P}}}$ is the Plummer core velocity dispersion, $b_{\rm P}$ is the Plummer scale length, σ is the local velocity dispersion, and $N \approx M_{\rm P}/\langle m \rangle$ is the number of bodies in the cluster. In normalizing $\langle r \rangle$ by $4b_{90}$,[4] we can probe how it relates to the χ_1 and χ_2 scalings employed in this work. To satisfy $R_1 < \langle r \rangle$, we must set $\chi_1 < \chi_{\rm r}$, where

$$\begin{aligned} \chi_{\rm r} = \frac{\langle r \rangle}{4b_{90}} &= \frac{1}{8} N^{2/3} \left(\frac{\sigma_{\rm c}}{\sigma}\right)^{4/3} \\ &= \frac{1}{8} \left[N \left(1 + \frac{r^2}{b_{\rm P}^2} \right) \right]^{2/3}, \end{aligned} \tag{20}$$

with r as the radial distance from the center of the Plummer cluster. If we limit our investigations to the core of

[4] An extra factor of two is added here so that we may consider $\langle r \rangle$ to be the maximal possible diameter of a spherical volume spanning an isolated encounter.

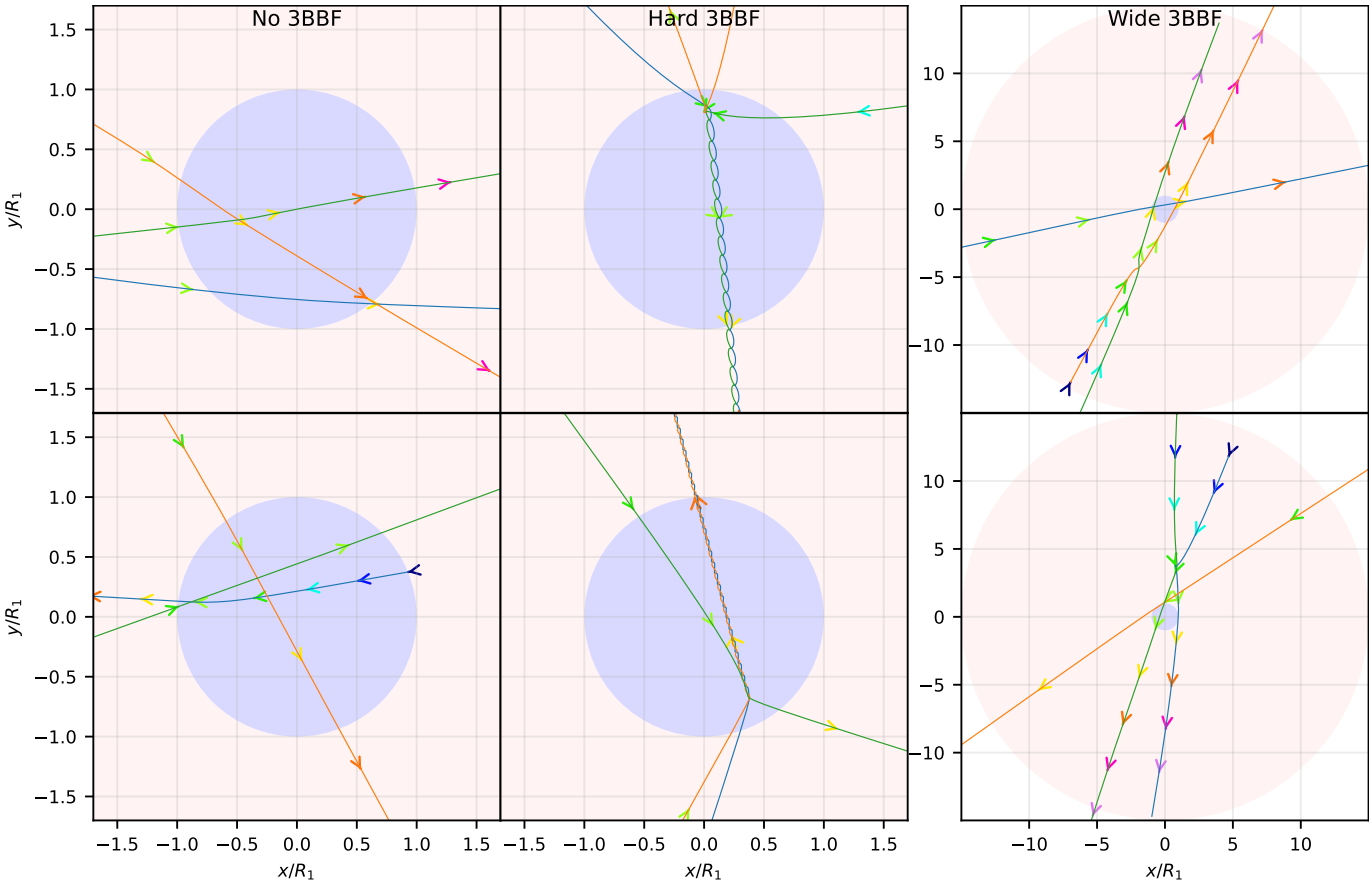

Figure 7. A 2D projection of six different equal-mass 3UB realizations. Each column corresponds to scatterings that result in (i) no, (ii) hard (here, $a \ll R_1$), or (iii) wide ($a > R_1$) 3BBF. The blue shaded region is the interaction volume of the initial condition algorithm (with radius R_1) and the red shaded region is defined by R_2; see Section 2.1 for details. Line color represents the trajectory of an individual body while color-coded arrows show the direction bodies are moving at uniformly selected color-coded time-steps in the simulation. The larger the spacing between arrows, the faster the body is moving. No resonant encounters occur here or in any 3UB simulation made yet.

a cluster, we find that $\chi_{\rm r} \approx 0.125\, N^{2/3}$ and that clusters consisting of $N = \{10^3, 10^4, 10^5, 10^6, 10^7\}$ bodies have a dimensionless $\chi_{\rm r} \approx \{13, 60, 270, 1250, 5800\}$, respectively. These choices of N span the typical range for open clusters to dense nuclear star clusters.

To choose an appropriate χ_1 for the rest of our analysis—and thereby enable more thorough examination of other important considerations for 3BBF—we take guidance from the above estimates surrounding $\chi_{\rm r}$ and Figures 4 and 5. In particular, the scalings of the 3BBF probabilities on χ_1 asymptotically settle into simple power laws at $\chi_1 \gtrsim 10$, allowing straightforward extrapolation in dynamically active environments that can sustain larger values of $10 < \chi_1 < \chi_{\rm r}$. Beyond this point, the properties of the binaries such as semi-major axis (normalized by R_1) and eccentricity no longer depend on χ_1.[5] We therefore choose to use a default value of $\chi_1 = 10$ in all our following analysis, unless noted otherwise. For this choice of χ_1, ≈0.7% of all 3UB initial conditions result in at least two of the three bodies already being energetically bound to each other. These 3UB initial conditions are rejected since we are interested in formation of *new* binaries. Although this rejection rate is larger than the typical 3BBF probability at $\chi_1 = 10$, our tests indicate that including scatterings where bodies are allowed to be bound at initialization does not significantly alter the soft or hard 3BBF probabilities in the equal and unequal mass cases. It follows that 3UB initial conditions in which two bodies are initiated especially close to one another are not a significant source of 3BBF. Our choice of $\chi_1 = 10$ therefore balances both accuracy and computational efficiency.

[5] We find this also holds for unequal mass simulations.

3.1.2. *Hard Binary Formation*

We now estimate the hard 3BBF rate in the equal point mass limit using the results of our analytically derived encounter rate—Equation (13)—and numerically

determined formation probabilities (Figure 4). We assert that the general solution to a numerically determined volumetric 3BBF rate is of the form

$$\tilde{\Gamma}^{\rm F}\left(<a,\chi_1\right) = P\left(<a,\chi_1\right)\tilde{\Gamma}_{\rm 3B}\left(\chi_1\right), \tag{21}$$

where $\tilde{\Gamma}_{\rm 3B}$ is the 3UB volumetric encounter rate and the 3BBF rate per 3UB encounter, $P\left(<a,\chi_1\right)$, is extracted from Figure 4.

Simplified for the case of identical bodies and velocity distributions, the volumetric encounter rate is

$$\tilde{\Gamma}_{\rm 3B} = \frac{2^{5/2}\pi^{3/2}}{3} n^3 R_1^5 \sigma. \tag{22}$$

The cumulative distribution of hard-binary SMA has the form $P(<a) \propto \left(a/a_{\rm fs}\right)^3$ when $a < R_1$. In Figure 4, the cumulative probability of forming binaries with $a/a_{\rm fs} \leq 1$ is

$$P(<a,\chi_1) \approx 1.85\times10^{-6}\left(\frac{\chi_1}{10}\right)^{-4.5}\left(\frac{a}{a_{\rm fs}}\right)^3. \tag{23}$$

Combining this probability with our encounter rate, the hard 3BBF rate for equal masses is

$$\tilde{\Gamma}^{\rm F}\left(<a,\chi_1\right) \approx 0.081\,\frac{G^5m^5n^3}{\sigma^9}\left(\frac{a}{a_{\rm fs}}\right)^3\chi_1^{1/2}. \tag{24}$$

Note that the $\chi_1^{1/2}$ dependency in Equation (24) highlights a unique environmental constraint on 3BBF rates not accounted for in any previous works. While the formation rate appears to be divergent—$\tilde{\Gamma}^{\rm F} \to \infty$ as $\chi_1 \to \infty$—this is contingent on the existence of an environment with an infinite average interparticle distance, a nonphysical consideration. Thus, to properly estimate a local 3BBF rate, a careful determination of the largest possible $\chi_1 < \chi_{\rm r}$ must be used in future (semi-)analytic prescriptions. Recently, Ginat & Perets (2024) corroborated our $\chi_1^{-4.5}$ probability scaling, finding an identical scaling by evaluating their analytic framework with their least stringent limiting condition on the 3UB interaction volume.

If we consider $\chi_1 = 10$ as a test case and redefine our hardness criteria in terms of the hard-soft boundary as defined by Goodman & Hut (1993), $a_{\rm hs} = \frac{Gm_1m_2}{2m\sigma^2}$ we may substitute $a_{\rm fs} \to \frac{2}{3}a_{\rm hs}$. The formation rate then becomes $\tilde{\Gamma}^{\rm F}\left(<a\right) \approx 0.86\,\frac{G^5m^5n^3}{\sigma^9}\left(\frac{a}{a_{\rm hs}}\right)^3$. The coefficient of 0.86 is a close match to the prediction of 0.75 from Goodman & Hut (1993) using detailed balance (and integrating their Equation 2.6 from $x/(m\sigma^2) : [1 \to \infty]$),

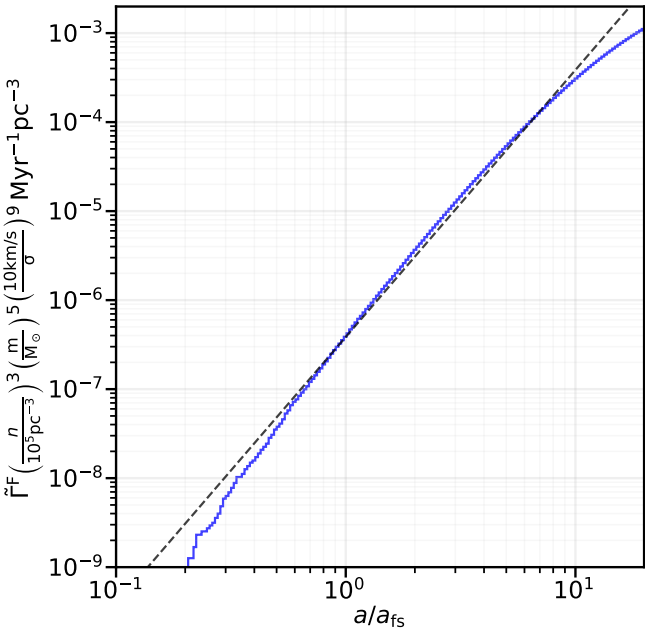

Figure 8. The estimated cumulative 3BBF rate for the interaction of three equal-mass bodies sampled from identical Maxwellian velocity distributions. Here, we show only the scattering experiments with dimensionless impact parameter $\chi_1 = 10$. The blue curve is a CDF of semi-major axis $(a/a_{\rm fs})$ scaled by Equation (17) and the black dashed line is a curve fit defined by Equation (24). The physical cross section for 3BBF increases with mass and decreases with speed since $R_1 \propto m/\sigma^2$. Our rate is within 15% of the rate predicted by Goodman & Hut (1993); see text near Equation (24).

sans the SMA and χ_1 scalings we have identified.[6] This semi-analytic expression for the 3BBF rate is displayed as a function of SMA in Figure 8 and over-plotted atop the numerical results for equal masses and $\chi_1 = 10$.

3.1.3. *Wide Binary Formation*

Soft binaries may also be described by the same scaling relations shown in the previous section so long as the parameter space of binary properties are restricted to $a < R_1$. The opposite limit—$a > R_1$—hosts properties exclusively describing the widest binaries that may form through 3BBF. These binaries follow an entirely different binary formation probability curve ($P \propto \chi_1^{-2}$) and their SMA and eccentricity distributions are not described by a simple power law, unlike in the hard binary limit. Given that binary SMA and eccentricity distributions are nearly independent of χ_1 for $\chi_1 \in [10, 100]$ (Figure 5), we may combine the scattering experiments

[6] Note that our formation rate is a "cumulative quantity" in that it expresses the rate of 3BBF of a minimum hardness; it is not a probability density function.

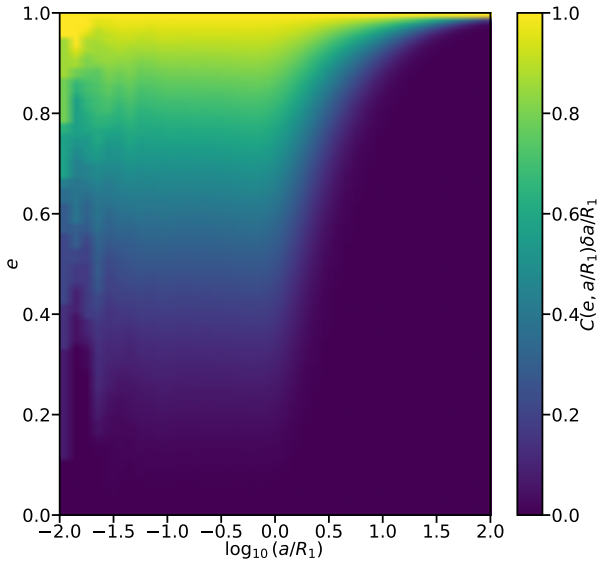

Figure 9. Heat map of binary eccentricity versus SMA (normalized by R_1, the radius of the interaction volume) across all 3BBF scatterings with $\chi_1 \geq 10$. Each (vertical) bin in SMA is normalized by the cumulative probability of binary formation in that bin $C(a/R_1)$. Eccentricity is thermal and roughly independent of SMA for $a/R_1 \lesssim 1$, but skews increasingly super-thermal with increasing a/R_1 for $a/R_1 \gtrsim 1$ ($\sim$98% of binaries).

spanning this interval to examine these binary properties at higher resolution. As a reminder, χ_1 represents a numerical factor chosen for convenience, with a maximal value dependent on environmental properties (e.g., the local average inter-particle separation).

Figure 9 is a two-dimensional heat map of the resulting SMA–eccentricity space from this combined dataset. The underlying density is normalized individually in each (vertical) bin in SMA to aid visualization of the eccentricity distribution for any given SMA. Figure 9 shows that the eccentricity distribution is roughly independent of SMA for $a/R_1 < 1$ (with some fluctuation attributable to low resolution at low SMA). However, for $a/R_1 > 1$, the binaries formed from 3BBF skew increasingly eccentric (super-thermal) as SMA increases, with the absolute softest binaries formed with a fixed interaction volume being exclusively super-thermal.

Following the same calculation as our hard binary formation rate from the previous section, the formation rate for super-thermal wide binaries crucially depends on the size of the interaction volume, R_1. Additionally, a power-law fit to the red curve in Figure 4 for $\chi_1 > 10$ yields a functional form for the overall 3BBF probability of $P \approx 4.2\chi_1^{-2}$. Since $\approx$85% of those binaries are wide (have $a > R_1$ in Figure 5), then the probability of forming a wide binary from 3BBF in the equal-mass limit at $\chi_1 > 10$ is roughly

$$P(a > R_1) \approx 3.6\chi_1^{-2} = 14.4\frac{b_{90}^2}{R_1^2} = 1.6\frac{G^2m^2}{\sigma^4 R_1^2}. \quad (25)$$

Combining this probability with equation 22, the volumetric 3BBF rate for (super-thermal) wide binaries in the equal-mass limit is

$$\tilde{\Gamma}^{\rm F}(a > R_1) \approx 16.8\frac{G^2m^2n^3}{\sigma^3}R_1^3. \quad (26)$$

Additionally, >50% of wide binaries have an SMA between $1 < a/R_1 < 5$ (see Figure 5).

The ability to realize a super-thermal, wide binary distribution is contingent on the dynamical properties of environments hosting 3BBF. Dynamically active and well-populated environments (e.g., star cluster cores) may enable many successful 3BBF events, but reasonably long-lived binaries form hard, with SMA smaller than the average inter-particle separation (i.e., $a < R_1 < \langle r_{\rm sep}\rangle$). Newly formed binaries with SMAs larger than the average inter-particle separation (and super-thermal eccentricities) are highly unlikely to persist within dense environments. In effect, binaries born within a central, dynamically active region should be thermal, independent of binary binding energy.

Yet, open clusters, star cluster halos, and stellar streams may not be so prohibitive (Peñarrubia 2021). The isotropically distributed recoil velocity experienced by all new binaries in 3BBF may quickly dissociate them from loose environments with low escape velocity, enabling the formation of binaries wider than the $\langle r_{\rm sep}\rangle$ of their original host. Thus, in contrast with other dynamical methods which do not explicitly investigate 3UB interactions (Hamilton & Modak 2023; Xu et al. 2023), the 3BBF mechanism may dynamically populate the super-thermal wide binaries observed by *Gaia* in the galactic field (Tokovinin 2020; Hwang et al. 2022).

3.2. *Unequal Point Masses*

We now report our findings on the first investigation of 3BBF for the case of unequal point masses. Just as in our equal-mass investigation, each body has an initial velocity randomly drawn from a single shared Maxwellian velocity distribution, with position and velocity basis vectors assigned according to our algorithm (see Section 2.1). In total, this dataset contains exactly 2.1×10^{10} simulations, or 10^9 scatterings per mass ratio combination.

Figure 10 summarizes our results. The top row is the 3BBF probability, $P_{\rm ij}$, as a function of mass ratio, $q_{\rm i}$. We explore the unequal-mass 3UB parameter space by transforming masses as: $(m_0, m_1, m_2) \rightarrow (q_0, q_1, q_2)$

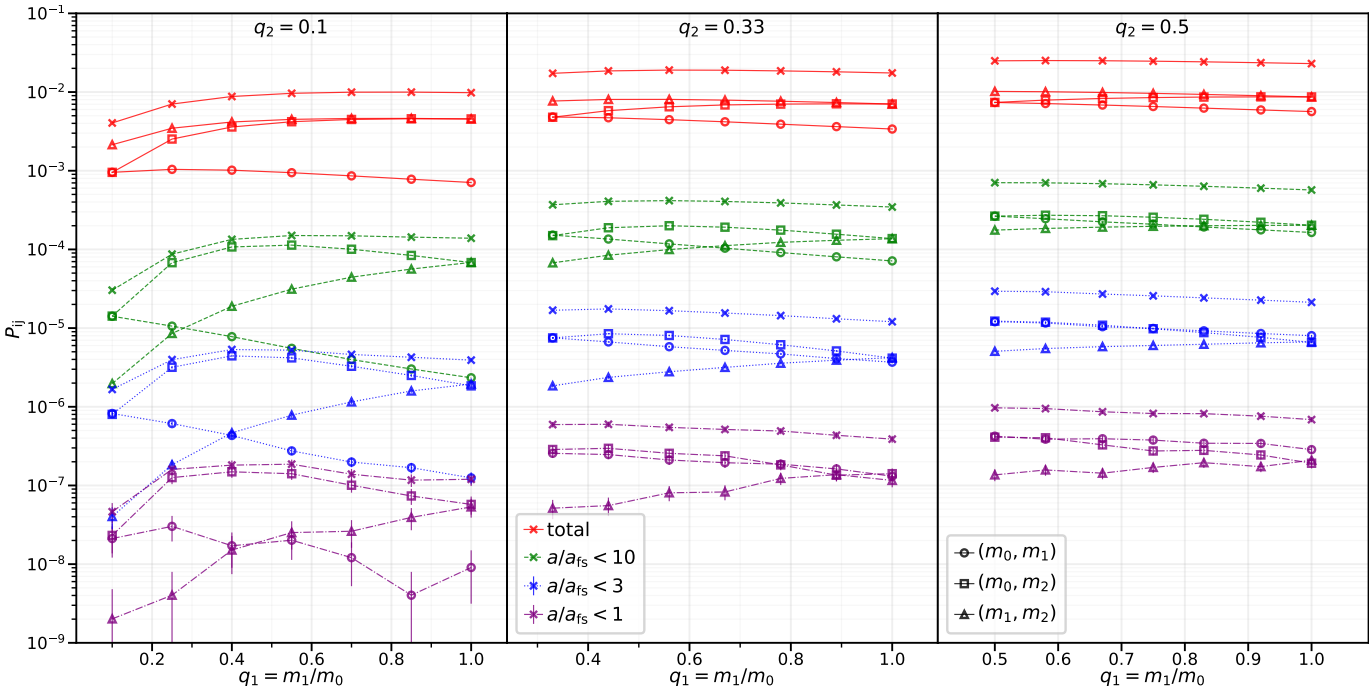

Figure 10. Probability of binary formation, P_{ij}, versus mass ratio of the second most massive body, $q_1 = m_1/m_0$. Mass ratios, $q_i = m_i/m_0$, are labeled in descending order by mass, with $q_0 = 1$ and $q_2 \leq q_1 \leq 1$. The 95% confidence intervals are included as error bars for all points under the assumption 3BBF is a Poissonian process. However, these error bars are difficult to see for any probability $\gtrsim 10^{-7}$ due to the large sample size (10^9 scatterings per value of χ_1). Accounting for hardness, we find that the pairing of the two most massive bodies is the least likely across the majority of the parameter space; the two least-massive bodies are the most likely pairing when allowing for binaries of arbitrarily large SMA. Each panel (column) shows P_{ij} for a different fixed $q_2 = m_2/m_0$. Color distinguishes binaries with the different minimum hardnesses specified in the legend while shapes indicate the three possible pairings of bodies. For most unequal mass ratios, new binaries typically contain the *least* massive body. The total 3BBF probability (cross-hatched curves for each color) increases with q_2 (i.e., as the mass ratios approach unity), regardless of binary hardness. See Table 1 for a numeric list of these probabilities and their counting uncertainties.

with $q_i = m_i/m_0$, $q_2 \leq q_1 \leq q_0$, and fixing $q_0 = 1$. Colors denote the minimum hardness ($a_{ij}/a_{fs,ij} < x$) of the binaries considered in each SMA bin while shapes separate binaries by the mass pairing $\{i, j\}$. The dimensionless impact parameter is fixed to $\chi_1 = 10$ for all experiments as we find that it balances resolution, efficiency, and accuracy throughout the entire parameter space (see Section 3.1).

A key assumption of 3BBF prescriptions in star cluster modeling codes such as `CMC` (e.g., Morscher et al. 2013, 2015) is that the two most massive bodies (q_0, q_1) in a 3UB encounter are the most likely to pair into a binary. Our findings unambiguously reject this assumption. Including binaries of any size, it is instead the two least massive bodies (q_1, q_2) which are the most likely to pair. The most plus least massive bodies (q_0, q_2) are the second most likely to pair generally, but the most likely in the hard binary limit. The pairing of (q_0, q_1) is the least likely 3BBF end-state independent of hardness, becoming orders-of-magnitude less likely as q_2 approaches the test particle limit. Naively, the tidal effect experienced between two bodies within the gravitational field of a third scales as $\left(\frac{m_k}{m_i+m_j}\right)^{1/3}$, where m_k is the mass of the perturbing body. So it is significantly easier for a more massive particle to perturb two low mass bodies than for a low mass body to perturb two high mass bodies. Stated differently, it is easier to change the energy/momentum of a less-massive body (less inertia), making it easier to extract two-body energy if the leftover single is more massive.

The differences in the pairing probabilities become increasingly subtle the closer in mass the three bodies are. For most of the explored parameter space, the pairing of (q_0, q_2) is the most probable hard binary pairing, with the most massive bodies (q_0, q_1) and least massive bodies (q_1, q_2) swapping prevalence as $q_1 \to 1$. As mass ratios approach unity, hard (q_0, q_1) pairings become more probable. Still, the pairing of the most massive bodies always comprises $< 50\%$ of total pairings, independent of hardness.

Turning to binary SMA and eccentricity distributions for fixed mass ratios (Figures 11 and 12), many

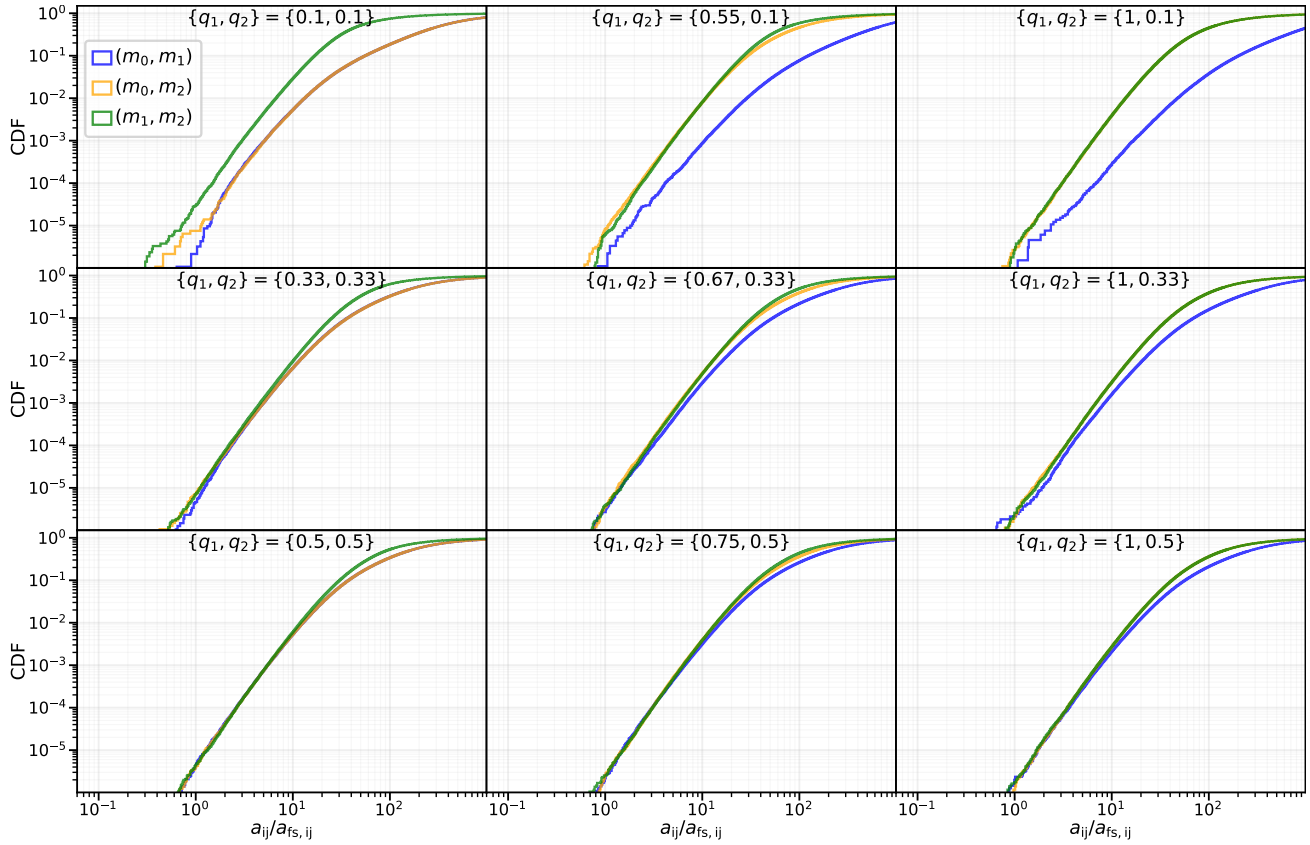

Figure 11. Binary SMA CDFs across various mass ratios with fixed velocity dispersion and $\chi_1 = 10$. Mass ratios, $q_{\rm i} = m_{\rm i}/m_0$ with $m_0 \geq m_1 \geq m_2$, are seen at the top of each subplot. Color specifies the pairing $\{q_{\rm i}, q_{\rm j}\}$ of each distribution. For $a_{\rm ij} < R_1$ (here, $R_1 = 2\chi_1 a_{\rm fs,01}$), the SMA distributions exhibit a simple power-law relation similar to the equal-mass case, but feature non-trivial deviations in the wide-binary limit ($a_{\rm ij} > R_1$).

of the tendencies occurring in equal-mass scattering are asymptotically emergent as binaries approach the fast/slow boundary. For the most extreme mass ratios ($q_2 = 0.1$), $C(a_{\rm ij}) \propto a_{\rm ij}^{2.5-3.0}$ and the SMA for the pairing of the most massive bodies (q_0, q_1) scales as $a_{01}^{2.5}$. As $q_2 \to 1$, all SMA distributions tend towards $C(a_{\rm ij}) \propto a_{\rm ij}^{3.0}$, as earlier identified in the case of equal masses.

Eccentricity distributions for binaries with $a_{\rm ij}/a_{\rm fs,ij} < 10$ follow an identical trend to what we identified with equal-mass encounters: they closely follow a thermal distribution. The only exception is the pairing of the two high-mass bodies, which yields a mildly super-thermal eccentricity distribution. Meanwhile, the eccentricity distributions for soft binaries are more extreme than in the case of equal-mass scattering. The soft pairing of (q_0, q_1) is extremely super-thermal ($\langle e_{01} \rangle \gtrsim 0.95$) while the soft pairing of (q_1, q_2) tends closer to a thermal distribution than in the equal-mass case.

4. PAIRING STARS AND BLACK HOLES

We now explore for the first time 3BBF between MS stars with masses $m_{\rm MS}/M_\odot : \{0.5, 1, 2\}$ and stellar mass BHs with masses $m_{\rm BH}/M\odot : \{20, 50, 100\}$. This is also the first study consider either relativistic or finite-size effects within the context of 3UB encounters. Additionally, we explore 3BBF between the encounter of: (i) two BHs and an MS star and (ii) two MS stars and a BH—mixed-species encounters that dominate 3BBF at most times in models of typical Milky Way globular clusters (e.g., Weatherford et al. 2023).

As in our point mass simulations, we fix the dimensionless impact parameter to be $\chi_1 = 10$ and draw the velocities of all bodies from a Maxwellian with a 1D velocity dispersion σ. In reality, species with such different masses will typically have different velocity distributions, but we leave nuanced exploration of this further complexity to future work to focus on the raw influence of mass ratio, along with relativistic and finite-size effects. However, variation in σ also varies the impact parameter since $R_1 \propto \sigma^{-2}$, so probes the strength of these effects in close passages. To show this impact clearly in our results, we therefore vary the velocities in the range

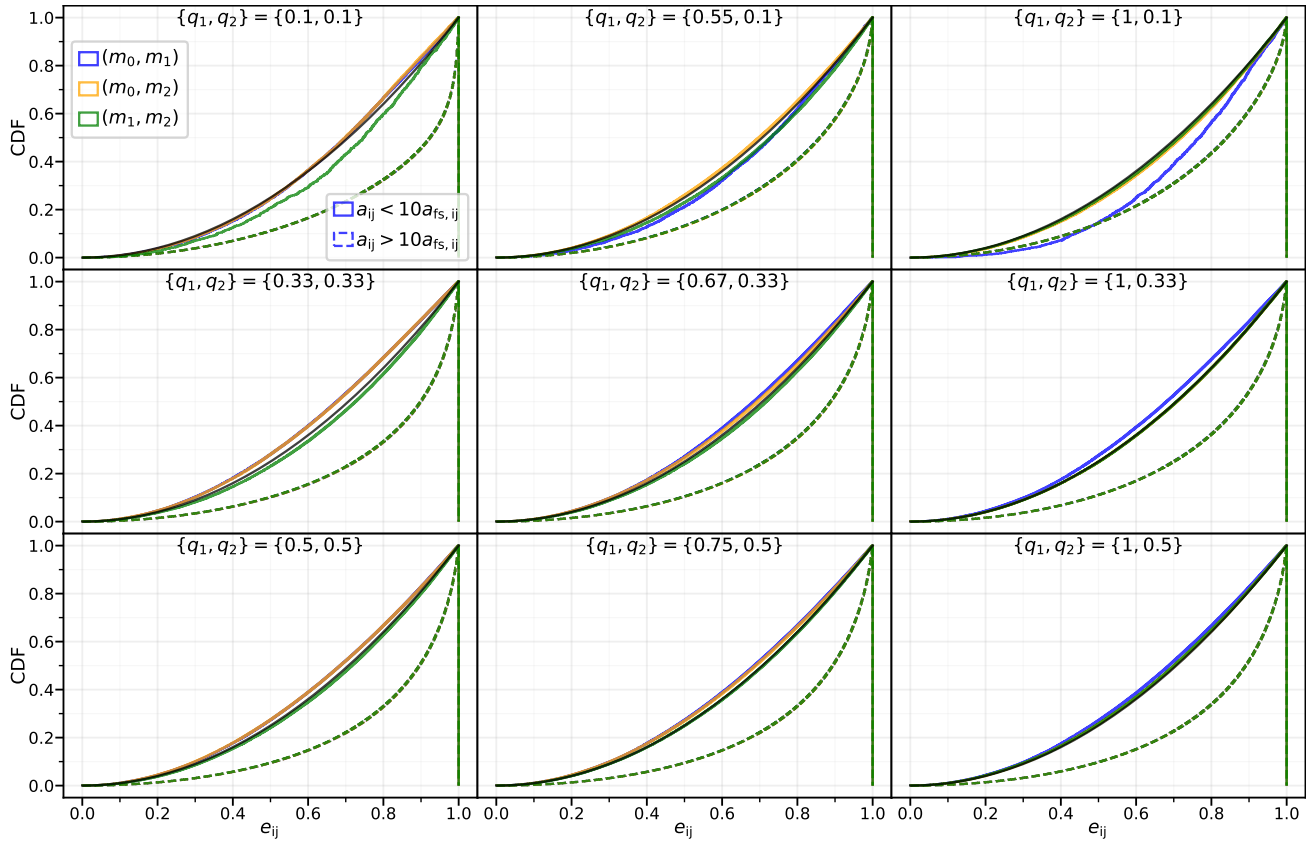

Figure 12. Binary eccentricity CDFs across various mass ratios with fixed velocity dispersion and $\chi_1 = 10$. Mass ratios, $q_i = m_i/m_0$ with $m_0 \geq m_1 \geq m_2$, are seen at the top of each subplot. Color specifies which two of the three bodies end up in the binary, numbered in decreasing order of their mass (0,1,2). The {solid, dashed} line style corresponds to binaries with SMA {greater, less} than $10a_{\rm fs,ij}$. Wide binaries, those with $a_{\rm ij} \gtrsim 10a_{\rm fs,ij}$, exhibit identical super-thermal eccentricity distributions across mass-pairings for fixed masses.

$\sigma \in [1, 300]\,{\rm km\,s^{-1}}$ for MS stars and $\sigma \in [3, 3000]\,{\rm km\,s^{-1}}$ for BHs. Varying mass to probe relativistic and finite-size effects effects is also an option, but the typical mass distributions of evolved MS stars and stellar-mass BHs in dense star clusters each span a smaller range than the typical local mean-squared velocities of the various dynamically active environments they may inhabit (e.g., open clusters to nuclear star clusters). Also, 3BBF rates scale more steeply with σ than with mass.

To explore the finite-size effects, we assign radii to stellar bodies according the classic MS radius relation (Demircan & Kahraman 1991),

$$r_{\rm i} = (m_{\rm i}/M_\odot)^{3/5} R_\odot. \tag{27}$$

To mitigate inaccuracies in the post-Newtonian (PN) approximation near the event horizon, BHs are assigned radii of 7 times their Schwarzschild radius,

$$r_{\rm i} = 14\frac{Gm_{\rm i}}{c^2}. \tag{28}$$

In all cases, collisions between stars are handled with the "sticky sphere" approximation, combining the masses (with no mass loss) once the surfaces of stellar bodies touch. The collison product is then placed instantaneously at the center-of-mass of the two former bodies with their center-of-mass velocity. BH mergers are treated with the numerical relativity prescriptions of Lousto & Zlochower (2013); Healy & Lousto (2018). Collisions between BHs and MS stars are resolved by placing the BH at the center-of-mass of the star–BH pair with their mutual center-of-mass velocity and assume no accretion (the star is destroyed). Under all circumstances, PN terms up to PN3.5 are enabled during integration and all BHs are assumed initially non-spinning. We do not include tidal physics in this first exploration of non-point-mass 3UB interactions, but we plan to explicitly explore such effects in a later work.

4.1. *Main-sequence Stars*

In Figure 13, we present our findings for 3UB interactions between equal-mass MS stars for three different cases: $m_{\rm i}/M_\odot = \{0.5, 1, 2\}$. The left panel shows the 3BBF probabilities as a function of σ, colors again

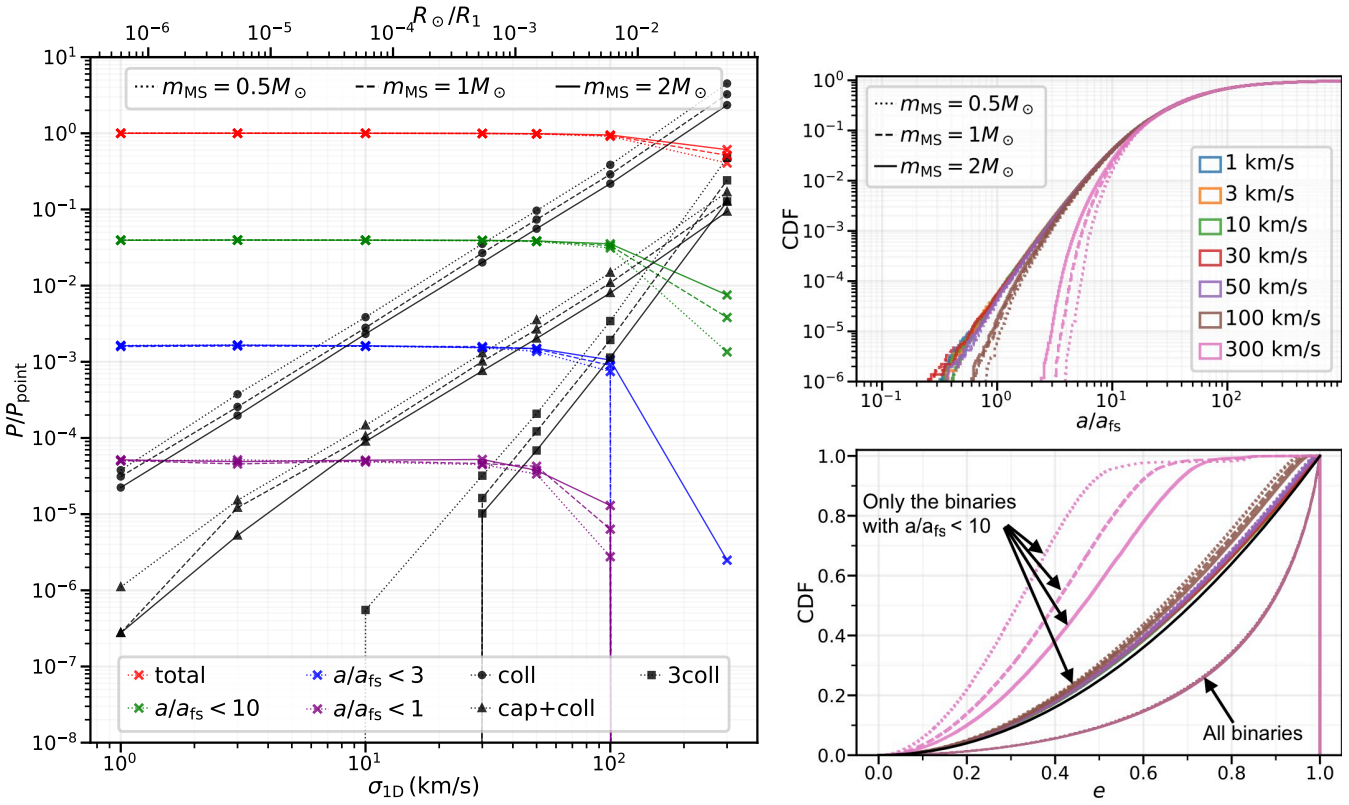

Figure 13. 3BBF distributions from scattering finite-sized bodies with main-sequence (MS) star radii, varying the 1D velocity dispersion σ and stellar mass but keeping $\chi_1 = 10$ fixed.
Left: Probability of 3BBF normalized by the total 3BBF probability (for $\chi_1 = 10$) in the earlier point mass scenario (red curve in Figure 4). Line style denotes the mass of the MS star, color again indicates binary hardness, while black indicates collision probabilities. The black labels are: **coll**—one collision, **cap+coll**—collision and capture of the third body, **3coll**—all three bodies collide during scattering. For most (but especially higher) velocities, collision probabilities exceed 3BBF probabilities. Even so, collisional effects negligibly reduce the 3BBF probability for $\sigma \lesssim 30\,\mathrm{km\,s^{-1}}$.
Right: Cumulative SMA and eccentricity distributions for each velocity dispersion. As reflected in the formation rates at left, the SMA distribution is roughly independent of σ until $\sigma \gtrsim 30\,\mathrm{km\,s^{-1}}$, where hard 3BBF becomes increasingly unlikely. Soft binaries are universally described by the same super-thermal eccentricity distribution (set of overlapping curves in the lower half of the eccentricity panel) independent of σ. Binaries with $a/a_{fs} < 10$ all closely follow a thermal eccentricity distribution (black curve) until the distributions become disrupted by the prevalence of collisions when $\sigma \gtrsim 30\,\mathrm{km\,s^{-1}}$, quickly suppressing formation of hard, eccentric binaries.

indicating binary hardness, with some additional black curves for collision probabilities (see caption). To better show the impact of finite size, we normalize the 3BBF probabilities by the total 3BBF probability (for $\chi_1 = 10$) in our equal point mass experiments from Section 3.1 (the red curve in Figure 4). The right panels of Figure 13 show the corresponding SMA and eccentricity distributions. In the lower panel, we show both the eccentricity distributions for all binaries regardless of SMA (lower set of overlapping curves), as well as only the subset of binaries with $a < 10a_{fs}$ (upper set of overlapping curves, predominantly found near the black curve representing a thermal distribution). Since it is dominated by wide binaries, the total binary population features the same super-thermal eccentricity distribution found in our the equal point mass experiments. This distribution does not depend on σ, as evidenced by the extreme degree of overlap of these curves. Meanwhile, the subset of binaries with $a < 10a_{fs}$ feature a nearly thermal eccentricity distribution, except at very high $\sigma \gtrsim 300\,\mathrm{km\,s^{-1}}$, where eccentricity instead skews significantly sub-thermal; solely due to eccentric binary periapse distances becoming comparable to MS stellar radii.

From the collision rates displayed in the left panel, it is immediately apparent that collisions are often orders of magnitude more common when compared to hard 3BBF ($P_{coll}/P_{hard} \in [10^0, 10^3]$). Yet, for all but the highest choices of σ (lowest R_1), the inclusion of finite-size collisional effects does not appreciably alter the 3BBF probability from the simpler point mass scenario.

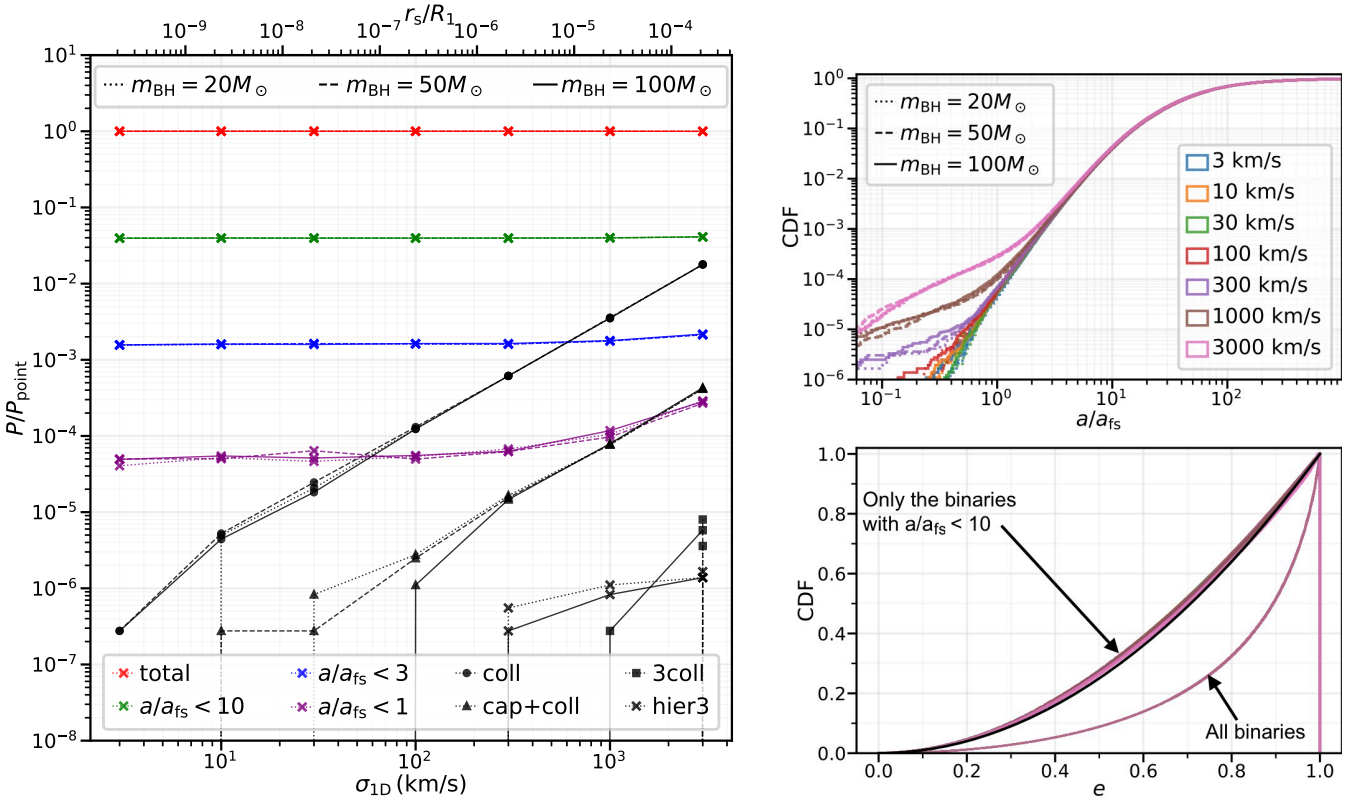

Figure 14. 3BBF distributions from scattering three equal-mass BHs, accounting for relativistic effects (post-Newtonian terms up to PN3.5) and varying the 1D velocity dispersion σ.
Left: 3BBF probability normalized by the total 3BBF probability (at $\chi_1 = 10$) in the point mass scenario (red curve in Figure 4). Line style denotes the mass of the BH, color represents hardness, and collision probabilities are in black. The black labels are: **coll**—one collision, **cap+coll**—collision and capture of the third body, **3coll**—all three bodies collide during scattering, **hier3**—formation of a hierarchical triple which lives for more than 10 orbital periods of the outer tertiary before the inner binary merges. BH mergers are far less common than MS mergers under identical velocity profiles. Relativistic effects never impede 3BBF probabilities, instead augmenting hard 3BBF when $\sigma \gtrsim 100\,\mathrm{km\,s^{-1}}$.
Right: Cumulative SMA and eccentricity distributions for each choice of velocity dispersion. As $\sigma \to c$, GW emission encourages BH binaries to form with smaller SMA. Soft binaries (set of overlapping curves in the lower half of the eccentricity panel) are universally described by the same super-thermal eccentricity distribution as in the point mass case. Binaries with $a/a_{fs} < 10$ all closely follow a thermal eccentricity distribution (black curve), independent of the relativistic effects present during 3BBF.

Changes to hard 3BBF specifically (purple) are statistically insignificant until $\sigma \gtrsim 30\,\mathrm{km\,s^{-1}}$, corresponding to $r_i/R_1 \gtrsim 10^{-4}$. Notably, this already exceeds σ at the center of typical globular clusters. Collisional suppression of 3BBF becomes relevant as the radius of the interaction volume, R_1, approaches $10^3\,R_\odot$. Changes to the SMA and eccentricity distributions at low σ are similarly negligible when compared to the point mass limit. At speeds high enough that the point mass and finite size scenarios strongly deviate from each other, the SMA and eccentricity deviations increase rapidly with σ (decreasing R_1). It is only when $\sigma \gtrsim 100\,\mathrm{km\,s^{-1}}$ that collisions severely hinder formation of especially hard and/or eccentric binaries. This may be relevant to nuclear star clusters, but not open or globular clusters.

Fixing velocity and χ_1, the radius R_1 of the interaction volume increases faster with mass than the radius r_i of MS stars. This can be seen from the proportion $R_1/r_i \propto m_i^{2/5}$ (equations (1) and (27)). Therefore, given identical velocity profiles, 3BBF involving more massive MS stars is less impeded by collisions—i.e., collisions in 3UB encounters are more frequent for lower-mass MS stars. The cross sections for two-body collisions and capture+collision events (two of the bodies colliding wth the collision product forming a binary with the third star) scale as $P \propto \sigma^2 \propto b_{90}^{-1}$. The probability of all three bodies colliding scales as $P \propto \sigma^4 \propto b_{90}^{-2}$.

That collisions arising from 3UB encounters do not significantly reduce the 3BBF rate from the point mass case reveals a fundamental aspect of 3BBF physics.

Namely, the overwhelming majority of initial configurations that align two-body trajectories into extremely tight periapse passages do *not* produce 3BBF in the point mass regime. Naturally, for finite-size bodies, such close passages result in collisions instead. This finding contradicts the intuition that if a tertiary body approaches two already strongly-interacting bodies, a tight binary will form. We have no evidence that this occurs in the 3BBF animations we have generated of hard or soft binary formation. Instead, our results strongly suggest that all three bodies "democratically" participate in a perturbative binary formation process.

4.2. *Black Holes*

Figure 14 presents the outcomes of 3UB interactions between three equal-mass BHs, accounting for relativistic effects, in three separate cases: $m_i/M_\odot = \{20, 50, 100\}$. Layout and line coloration/style are identical to Figure 13 for MS stars. All 3BBF probabilities in the left panel are again normalized by the total 3BBF probability for equal point masses (at $\chi_1 = 10$) in Section 3.1. As expected, accounting for relativistic effects changes negligibly the 3BBF probability from the Newtonian point mass scenario except in the case of hard binaries (purple) at high $\sigma \gtrsim 300\,\mathrm{km\,s^{-1}}$ ($r_s/R_1 \gtrsim 10^{-6}$). It is also clear from the collision rates (black) that BH mergers are far less likely than collisions between typical MS stars for identical velocities. This is a natural result of the minuscule physical cross-section for two-body GW capture compared to the (relatively enormous) physical radius of MS stars of identical velocity. Using the GW capture radius, $r_{\rm p,GW}$, from Quinlan & Shapiro (1989), we find that $r_{\rm p,GW}/R_1 \propto (\sigma/v)^{10/7}$. This is precisely the scaling with σ that we find for the probabilities of collision (**coll**; black circles) and capture+collision (**cap+coll**; black triangles).

Additionally, the scalings with σ of the 3BBF and collision probabilities are independent of mass since $r_{\rm s}$ and R_1 both scale $\propto m$ with $r_{\rm i}/R_1 = 0.3(\sigma/c)^2$. In other words, relativistic deviations from the point mass scenario scale only in powers of v/c. These relativistic deviations do not begin to peak above numerical noise until $\sigma \gtrsim 100\,\mathrm{km\,s^{-1}}$ (i.e., $\sigma/c \gtrsim 10^{-4}$), observable in the subtle boost to the hardest portion of the SMA distribution, becoming more dramatic as $\sigma/c \to 1$. We find no deviation in eccentricity distributions in comparison to point mass interactions. Thus, hard 3BBF with BHs is well-described by a thermal eccentricity distribution.

We are also excited to report a small probability in which three unbound BHs may undergo a 3UB interaction that produces a hierarchical triple via GW emission. Though most capture+collision end-states (**cap+coll**) involve the formation of a short-lived triple BH system, we only classify outcomes as a hierarchical triple (**hier3**; black crosses) when the hierarchy survives for $\tau \gtrsim 10$ orbital periods of the outer tertiary before the inner binary merges. A binary BH containing a second-generation BH merger product is always left behind in these equal-mass, zero-spin scenarios due to the nonexistence of GW recoil kicks in such a case. However, we stress that this is an extremely rare occurrence and is poorly resolved, even for environments with a local velocity dispersion in excess of $1000\,\mathrm{km\,s^{-1}}$.

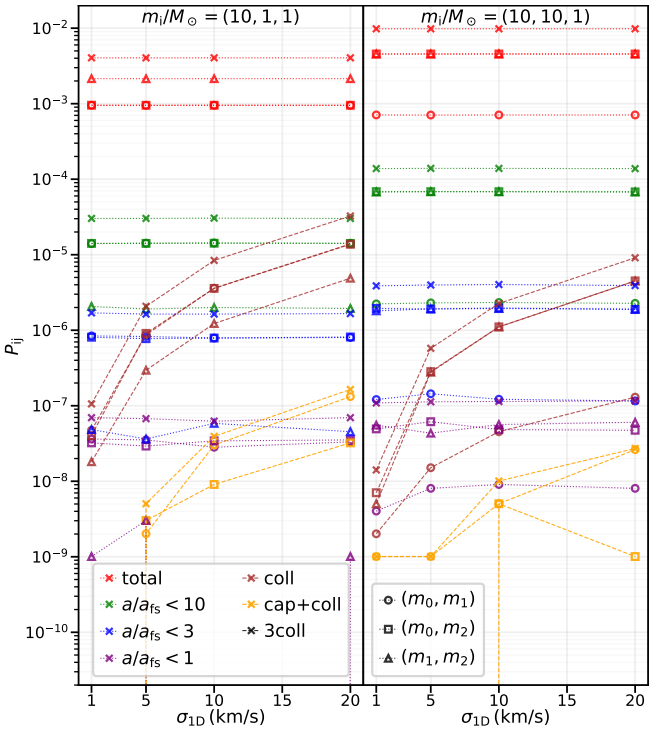

Figure 15. 3BBF probabilities (non-normalized) between (*left*) a BH and two MS stars and (*right*) two BHs and an MS star with $\chi_1 = 10$. All BHs (initially non-spinning) have mass $10\,M_\odot$ and all MS stars have mass $1\,M_\odot$. These scattering experiments are thus the finite-sized, relativistic equivalent of the earlier simulation sets for unequal masses with $q_{\rm i} = \{1, 0.1, 0.1\}$ (left) and $q_{\rm i} = \{1, 1, 0.1\}$ (right), respectively. Specific binary pairing combinations are identified by shape as in Figure 10. Colors distinguish 3BBF resulting in different binary hardness, as well as several different collision probabilities (labeled as in Figures 13 and 14). We find that 3BBF rates are largely unchanged compared to the Newtonian point mass limit, but direct collisions occur more frequently as the local velocity dispersion increases. Tidal disruption events should be even more frequent since they have a larger cross section compared to direct BH–star collisions.

4.3. *Main-sequence Stars and Black Holes*

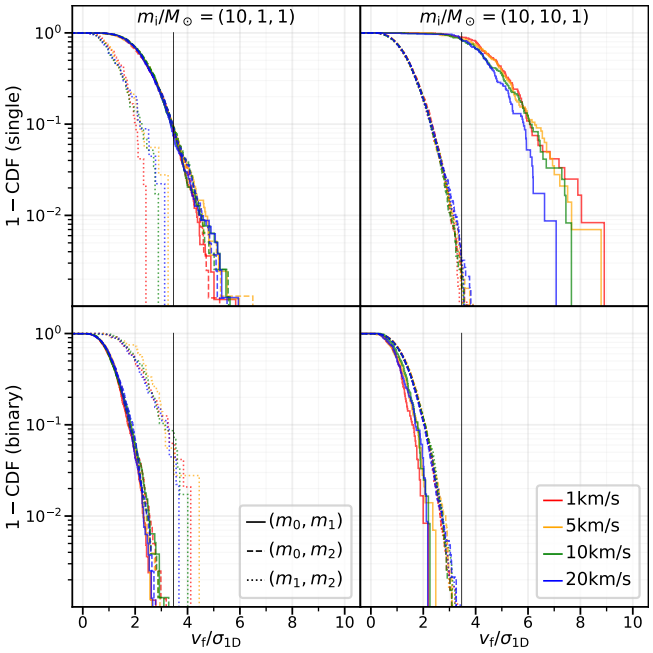

Figure 16. Survival function $(1 - C(v_f/\sigma))$ for the final velocity (v_f/σ) of the catalyzing single (*top row*) and binary (*bottom row*). These distributions include only the binaries formed with $a_{ij}/a_{fs,ij} < 3$. Color and line style illustrate the velocity dispersion and specific mass pairing, respectively. The vertical black line at $v_f/\sigma = 2\sqrt{3}$ denotes the escape velocity from the core of a Plummer cluster.

A key application of 3UB encounters is the scenario involving MS stars ($\sim 1\,M_\odot$) and stellar-mass BHs ($\sim 10\,M_\odot$) within the cores of dense star clusters. Weatherford et al. (2023) recently demonstrated that such encounters dominate 3BBF at most times in typical Milky Way globular clusters (those retaining significant BH populations). They also found that such interactions may dominate high-speed ejection ($\Delta v_k > \sigma$) from such clusters due to the recoil experienced by the leftover single, expected to typically be a low-mass MS star. However, the frequency of high-speed ejection and the identity of the ejected body (i.e., high-mass or low-mass object, single or binary) may be conditional on previously unexplored unequal-mass, finite-size, and relativistic effects.

In Figure 15, we reaffirm that physical collisions, despite being more frequent than hard 3BBF, do not significantly suppress hard 3BBF when compared to the point mass scenario for the unequal masses (and velocity dispersions; $\sigma \in [1, 20]\,\mathrm{km\,s^{-1}}$) explored here. This result is consistent with our findings in Sections 4.1 and 4.2 that high-σ environments are necessary to significantly suppress hard 3BBF among equal-mass MS stars ($\sigma \gtrsim 30\,\mathrm{km\,s^{-1}}$) or BHs ($\sigma \gtrsim 100\,\mathrm{km\,s^{-1}}$).

BH–star 3BBF rates for both mass combinations are unchanged compared to the Newtonian point mass scenario (see Figure 10), but the collision rate is substantial. As we demonstrated in Section 4.1, initial configurations that produce collisions are more frequent than hard 3BBF when scattering finite-sized bodies. However, these initial states are non-degenerate for typical cluster velocity dispersions; i.e., an initial state that produces a hard binary in the point mass regime does not necessarily produce a collision during an identical encounter with finite-size bodies. An unexpected consequence follows if we consider that the tidal disruption radius is about 2.2 times larger than the BH–star collision radius between a $10\,M_\odot$ BH and a $1\,M_\odot$ MS star ($r_t = r_*\,(m_{BH}/m_*)^{1/3}$). Namely, the number of BH–star tidal disruption events may be between 2 to 5 times higher than the direct collision rate, contingent on the subtleties of 3UB gravitational focusing. While direct BH–star collisions do not meaningfully suppress the hard 3BBF rate, we are uncertain whether tidal disruption events would yield significant suppression. Regardless, these results suggest 3UB encounters may provide a substantial boost to the predicted frequency of transient tidal/collisional phenomena in the cores of dense star clusters.

In Figure 16, we also examine the final velocity v_f of binaries and the leftover (catalyzing) singles produced by 3BBF from the above setup (i.e., BHs of mass $10\,M_\odot$ and MS stars of mass $1\,M_\odot$). Note the velocities shown are in the frame of the interaction volume, akin to the global reference frame of the host environment, not the center-of-mass frame of the three bodies. The primary advantage is the direct translation to the final velocity of each body within its host environment. We also only include in the analysis binaries formed with $a_{ij}/a_{fs} \leq 3$—i.e., hard and slightly wider binaries.

Given our assumption that the bodies' velocities are drawn from the same distribution regardless of mass, we find it is excessively rare that newly formed BH–MS or BH–BH *binaries* have a final velocity in excess of the escape velocity ($v_{esc} = 2\sqrt{3}\sigma$) of a Plummer core with the same characteristic velocity dispersion. Even in the favorable case where a (heavy) BH catalyzes the formation of a (light) MS–MS binary with $a_{12}/a_{fs} \leq 3$, ejection of the binary only occurs <5% of the time. Notably, Figure 15 shows that the MS–MS pairing in such a case is also 10 times *less* likely than a BH–MS pairing, for which ejection of the binary would be even harder. Weatherford et al. (2023) similarly predicted that the energy release from 3BBF alone is almost never directly responsible for the ejection of a binary. Notably, the simplified 3BBF prescription from the `CMC` code used in

that study automatically pairs the most massive bodies, artificially making binary ejection even more unlikely than the otherwise small fraction found here.

From simple momentum conservation, the prospect of low-mass catalysts experiencing high-speed kicks from 3BBF is much more promising. When an MS star catalyzes the formation of a BH–MS or BH–BH binary with $a_{\rm ij} \leq 3a_{\rm fs,ij}$, $\sim$10% and $\sim$90% of MS star catalysts have final velocities $v_{\rm f} > v_{\rm esc}$, respectively. Hard 3BBF can lead to even higher ejection speeds for single stars as $v_{\rm f} \propto \sigma$ if we only consider point-mass Newtonian mechanics. As discussed in Section 4, by adding finite-size considerations, direct collisions between stars with masses of $\sim 1\,M_\odot$ begin to reduce 3BBF for velocity dispersions between 30–50 $\rm km\,s^{-1}$ and eliminate hard 3BBF at $\sigma > 100\,\rm km\,s^{-1}$. This reduction in 3BBF rates due to collisions is less pronounced for more massive bodies since the size of the interaction volume increases faster than the physical radii of interacting stars.

At an order-of-magnitude level, these results are consistent with the velocity distribution from MS star ejecta via 3BBF in `CMC` (Weatherford et al. 2023). There are a variety of complexities that need to be further explored to make a more rigorous comparison, however. For example, the initial velocities of the bodies in Figure 16 are sampled from the local velocity dispersion (typical velocity), while successful 3BBF ejecta from Weatherford et al. (2023) should naturally be skewed to (higher) initial velocities already near to $v_{\rm esc}$. Furthermore, Figure 16 does not account for species of different mass having different σ; nor does it account for the full distribution of mass ratios and relative velocity ratios found in typical 3UB encounters in the core of a dense star cluster. We leave a more rigorous analysis of such considerations to future work.

Finally, as mentioned earlier, tidal physics will likely modify the final velocity of the catalyst. For example, Kremer et al. (2022) demonstrated that velocity kicks applied to stellar remnants following tidal disruption events (due to asymmetric mass loss) may exceed $\sim$200 $\rm km\,s^{-1}$ when the mass of the BH is at least 10 times greater than the star's mass. So the prospect of impulsive acceleration to high speed during a 3UB encounter is likely much higher than suggested by our results accounting only for (post-)Newtonian dynamics. Along with Figure 16, we find that 3UB encounters should contribute to the ejection of runaway stars (and possibly even hypervelocity stars) from globular clusters, supporting Weatherford et al. (2023). Conclusively demonstrating that 3BBF dominates the production of such ejecta over other binary-mediated channels requires further numerical examination of the 3BBF rate for realistic velocity and mass distributions in globular clusters. This is especially true when considering hypervelocity ejecta, which fundamentally would result from encounters deep in the tail of the 3BBF kick velocity distribution.

5. SUMMARY AND FUTURE WORK

5.1. *Summary*

We have explored the formation of new binaries from three unbound bodies in greater detail than any prior efforts, including the first study of 3BBF to feature unequal masses, finite-size effects, and post-Newtonian effects. Specifically, we study 3BBF by running $>3\times10^{10}$ three-body scattering experiments with the state-of-the-art direct N-body integrator Tsunami. After reproducing the canonical 3BBF scattering experiments of AH76, we correct an oversight in their algorithm (adopted from Agekyan & Anosova 1971) related to spherical symmetry. With this correction and a new analytic encounter rate for 3BBF, we compute a hard 3BBF rate that agrees well with Goodman & Hut (1993) in the case of equal-mass bodies; see Equation (24). We also confirm that 3BBF is almost exclusively an impulsive phenomenon. Resonant encounters leading to 3BBF are extremely disfavored due to the total positive energy of three unbound bodies, preventing a three-body bound state from occurring without dissipation (e.g., gravitational radiation or collisions). Additional key results are as follows:

1. Newly formed binaries from 3BBF are overwhelming soft, in agreement with AH76 and Goodman & Hut (1993). We find that the cumulative distribution of binary semi-major axis, a, scales as a^3—notably shallower than the $a^{5.5}$ scaling of 3BBF recipes in Monte Carlo star cluster modeling (e.g., `CMC`; Rodriguez et al. 2022). Typical SMA also grows with dimensionless impact parameter χ_1, so larger interaction volumes lead to both wider binaries and higher 3BBF rates (since 3UB encounter rates scale as χ_1^5). This has dramatic implications for star cluster dynamics since soft binaries are often assumed to disrupt too quickly to affect cluster evolution. Yet Goodman & Hut (1993) estimate $\gtrsim$90% of long-lived binaries form soft; they are simply the rare few of many soft binaries from 3BBF that survived and hardened. So neglect of soft 3BBF in cluster modeling may warrant re-examination.

2. Wide binaries from 3BBF have super-thermal eccentricities. Since most binaries form soft, this implies that soft 3BBF may produce the eccentric

wide binaries observed with *Gaia* (e.g., Tokovinin 2020; Hwang et al. 2022). Star clusters may therefore be robust sources of eccentric wide binaries. In particular, such binaries may form via 3BBF interactions in short-lived or dissolving clusters (though this likely results in a thermal eccentricity distribution, e.g., Kouwenhoven et al. 2010), or perhaps in the extended tidal tails of more massive clusters. Although the local density in tidal tails is significantly lower than in the core of a star cluster, the highly-correlated epicyclic trajectories of slow escapers in tidal tails may produce exceptionally low relative velocities between neighboring bodies conducive to wide 3BBF; recall the 3BBF rate depends much more steeply on relative velocity than on density. Survival of newly-formed wide binaries and their deposition into the Galactic field may also be easier in this case, and the extreme velocity anistropy in tidal tails may result in significantly different semi-major axis or eccentricity distributions than expected from an isotropic assumption for 3BBF (as in this paper). We shall examine such prospects in future work.

3. Independent of mass ratio, the eccentricity distribution of hard binaries formed through 3BBF is universally well-described by the classic thermal distribution (e.g., Jeans 1919; Heggie 1975). This likely occurs because an isotropically distributed sea of gravitating bodies will fully explore phase space, analogous to how resonant binary-single encounters fully explore phase space in the aforementioned texts. The a^3 scaling of the cumulative distribution for SMA also holds for hard binaries in most cases; a key exception is the (unlikely) pairing of two massive bodies by a low-mass catalyst.

4. Exploring unequal-mass 3BBF for the first time, our results refute the common assumption that the two most massive bodies are the most likely to pair (e.g., Morscher et al. 2013). Instead, the two least massive bodies pair most frequently in soft/wide binaries while the most massive plus least massive bodies pair most frequently in hard binaries. Only for mass ratios near unity are the two most massive bodies likely to pair (up to ≈40% of hard 3BBFs).

5. Physical stellar collisions are a more likely outcome of a 3UB encounter than hard binary formation for MS stars with velocities $\sigma > 1\,\mathrm{km\,s^{-1}}$. Yet the collisions do not significantly suppress 3BBF among MS stars (relative to the point mass limit) at velocity dispersions $\lesssim 30\,\mathrm{km\,s^{-1}}$. This implies that the initial states leading to stellar collisions in 3UB interactions are largely separate from those leading to hard binary formation.

6. Post-Newtonian effects can promote hard binary BH formation through gravitational wave emission during close high-speed approach. Yet such enhancement (and prevalence of BH mergers) is only significant for $\sigma \gtrsim 100\,\mathrm{km\,s^{-1}}$, likely only relevant in nuclear star clusters. In such high-σ environments, the probability of forming short-lived hierarchical triples through 3UB BH scattering can also be significant, surpassing the hard 3BBF probability. Formation of longer-lived triples (surviving for at least several orbits of the outer tertiary) remains rarer than hard 3BBF, even when $\sigma \gtrsim 1000\,\mathrm{km\,s^{-1}}$.

7. The above results hold for mixed-species interactions between stellar-mass BHs and MS stars, the dominant type of 3UB encounters in star cluster models (Weatherford et al. 2023). For typical masses and velocities in globular clusters, neither direct collisions nor post-Newtonian effects significantly alter 3BBF rates in this case relative to the limit of Newtonian point masses. As with MS stars alone, BH–star collisions in these mixed-species encounters are much more common than hard binary formation, but do not significantly suppress 3BBF. Since the cross section for a tidal disruption event (TDE) is larger than for a direct BH–star collision, 3UB encounters in star clusters may be a significant source of TDEs.

8. We confirm that 3BBF can eject bodies from star clusters at speeds at least a few times their central escape velocity (depending on the mass ratios in the encounter). In particular, when a MS star catalyzes the production of a typical hard BH–MS or BH–BH binary, ∼10% and ∼90%, respectively, of the MS catalysts exit the 3UB encounter fast enough to escape their host cluster. 3BBF in star clusters may therefore contribute to runaway stars in the Galactic halo, but at rates that remain uncertain pending future work that more closely examines 3BBF in a background environment with fully realistic mass and velocity distributions. Tidal disruption physics may further enhance high-speed ejection from 3BBF since asymmetric mass loss imparts an additional kick to the stripped star (Kremer et al. 2022). Newly formed *binaries* rarely exit 3BBF events with sufficient speed to escape from the center of a star cluster, even when the catalyst is much more massive than the binary.

9. Finally, our results agree with an independent analytical investigation of 3BBF by Ginat & Perets (2024), submitted during the review process of this work. In particular, Ginat & Perets (2024) developed a statistical analytic theory investigating the probabilities of 3BBF and the distributions of orbital parameters in the equal-mass case and agree that 3BBF is a promising source of wide eccentric binaries. They also corroborated that the 3BBF probability for binaries formed with SMA less than their strong interaction region (i.e., $a < R_1$) scales as $P_{\rm ij} \propto \chi_1^{-4.5}$ and that these binaries have an approximately thermal eccentricity distribution. They also corroborate that soft, wide binaries feature a super-thermal eccentricity distribution.

5.2. *Future Work*

Despite having touched on some of the more extreme regimes of the 3UB parameter space in this work, the overwhelming majority is yet to be explored (e.g., varying velocity ratios, non-isotropic environments, energy partitioning). Given the number of other considerations investigated here, these regimes are beyond the scope of this work, but may dramatically impact binary properties.

Proper treatment of tidal physics in the close passages of stars, including tidal disruption events, in 3UB scattering may be impactful and requires focused study. In particular, our results in Section 4.3 demonstrate that direct BH–star collisions do not meaningfully reduce the rate of hard binary formation, yet they are a *more common* outcome. The complex interplay between tidal physics and hard binary formation is yet to be explored, but we do know the tidal disruption rate will be at least twice as frequent as the collision rate—if only due to gravitational focusing. It immediately follows that tidal disruption events are likely highly prevalent in 3UB encounters within dense stellar clusters. Additionally, future studies will be targeted towards specific environments, enabling us to make concrete and practical environment-specific 3BBF rate predictions.

In total, our results should serve as a reminder that the 3UB problem is largely unexplored. Expectations concerning populations of dynamically assembled binaries may change significantly when a proper treatment of arbitrary mass-ratio 3UB scattering is incorporated into Monte Carlo star cluster modeling codes such as `CMC`. While 3BBF features obvious applications in constraining the history of dynamically assembled compact-object binaries and their subsequent mergers observable through gravitational waves, the potential for enhancing our understanding of "traditional" stellar binary formation provides further incentive for renewing investigations into 3BBF as a critical topic in dynamical astrophysics.

ACKNOWLEDGEMENTS

This work was supported by NSF Grant AST-2108624 at Northwestern University. A.A.T. acknowledges support from the European Union's Horizon 2020 and Horizon Europe research and innovation programs under the Marie Skłodowska-Curie grant agreements No. 847523 and 101103134. We thank Barry Ginat for informative and positive conversations regarding their analytic analysis of 3BBF and Yoram Lithwick, Mike Zevin, Kyle Kremer, Chris Hamilton, and Jeff Andrews for insightful discussions regarding numerical sampling methods and astrophysical implications. This work was supported through the computational resources and staff contributions provided for the Quest high-performance computing facility at Northwestern University. Quest is jointly supported by the Office of the Provost, the Office for Research, and Northwestern University Information Technology. DA also acknowledges support from a CIERA Board of Visitors Fellowship and the computing resources at CIERA funded by NSF Grant PHY-1726951.

REFERENCES

Aarseth, S. J., & Heggie, D. C. 1976, A&A, 53, 259

Agekyan, T. A., & Anosova, Z. P. 1971, Soviet Ast., 15, 411

Arca Sedda, M., Kamlah, A. W. H., Spurzem, R., et al. 2023, MNRAS, 526, 429, doi: 10.1093/mnras/stad2292

Atallah, D., Trani, A. A., Kremer, K., et al. 2023, MNRAS, 523, 4227, doi: 10.1093/mnras/stad1634

Bacon, D., Sigurdsson, S., & Davies, M. B. 1996, MNRAS, 281, 830, doi: 10.1093/mnras/281.3.830

Banerjee, S., Baumgardt, H., & Kroupa, P. 2010, MNRAS, 402, 371, doi: 10.1111/j.1365-2966.2009.15880.x

Binney, J., & Tremaine, S. 2008, Galactic Dynamics: Second Edition

Chernoff, D. F., & Huang, X. 1996, in Dynamical Evolution of Star Clusters: Confrontation of Theory and Observations, ed. P. Hut & J. Makino, Vol. 174, 263

Demircan, O., & Kahraman, G. 1991, Ap&SS, 181, 313, doi: 10.1007/BF00639097

Fabian, A. C., Pringle, J. E., & Rees, M. J. 1975, MNRAS, 172, 15, doi: 10.1093/mnras/172.1.15P

Fregeau, J. M., Cheung, P., Portegies Zwart, S. F., & Rasio, F. A. 2004a, MNRAS, 352, 1, doi: 10.1111/j.1365-2966.2004.07914.x

—. 2004b, MNRAS, 352, 1, doi: 10.1111/j.1365-2966.2004.07914.x

Fregeau, J. M., Gürkan, M. A., Joshi, K. J., & Rasio, F. A. 2003, ApJ, 593, 772, doi: 10.1086/376593

Freitag, M., & Benz, W. 2001, A&A, 375, 711, doi: 10.1051/0004-6361:20010706

Generozov, A., Stone, N. C., Metzger, B. D., & Ostriker, J. P. 2018, MNRAS, 478, 4030, doi: 10.1093/mnras/sty1262

Ginat, Y. B., & Perets, H. B. 2024, arXiv e-prints, arXiv:2404.08040, doi: 10.48550/arXiv.2404.08040

Goodman, J., & Hernquist, L. 1991, ApJ, 378, 637, doi: 10.1086/170464

Goodman, J., & Hut, P. 1993, ApJ, 403, 271, doi: 10.1086/172200

Hamilton, C., & Modak, S. 2023, arXiv e-prints, arXiv:2311.04352, doi: 10.48550/arXiv.2311.04352

Healy, J., & Lousto, C. O. 2018, PhRvD, 97, 084002, doi: 10.1103/PhysRevD.97.084002

Heggie, D., & Hut, P. 2003, The Gravitational Million-Body Problem: A Multidisciplinary Approach to Star Cluster Dynamics

Heggie, D. C. 1975, MNRAS, 173, 729, doi: 10.1093/mnras/173.3.729

Hills, J. G. 1990, AJ, 99, 979, doi: 10.1086/115388

Hut, P. 1985, in Dynamics of Star Clusters, ed. J. Goodman & P. Hut, Vol. 113, 231–247

Hut, P., & Inagaki, S. 1985, ApJ, 298, 502, doi: 10.1086/163636

Hut, P., McMillan, S., & Romani, R. W. 1992, ApJ, 389, 527, doi: 10.1086/171229

Hwang, H.-C., Ting, Y.-S., & Zakamska, N. L. 2022, MNRAS, 512, 3383, doi: 10.1093/mnras/stac675

Ivanova, N., Belczynski, K., Fregeau, J. M., & Rasio, F. A. 2005, MNRAS, 358, 572, doi: 10.1111/j.1365-2966.2005.08804.x

Ivanova, N., Chaichenets, S., Fregeau, J., et al. 2010, ApJ, 717, 948, doi: 10.1088/0004-637X/717/2/948

Jeans, J. H. 1919, MNRAS, 79, 408, doi: 10.1093/mnras/79.6.408

Joshi, K. J., Nave, C. P., & Rasio, F. A. 2001, ApJ, 550, 691, doi: 10.1086/319771

Joshi, K. J., Rasio, F. A., & Portegies Zwart, S. 2000, ApJ, 540, 969, doi: 10.1086/309350

Kouwenhoven, M. B. N., Goodwin, S. P., Parker, R. J., et al. 2010, MNRAS, 404, 1835, doi: 10.1111/j.1365-2966.2010.16399.x

Kremer, K., Lombardi, J. C., Lu, W., Piro, A. L., & Rasio, F. A. 2022, ApJ, 933, 203, doi: 10.3847/1538-4357/ac714f

Kremer, K., Piro, A. L., & Li, D. 2021, ApJL, 917, L11, doi: 10.3847/2041-8213/ac13a0

Kulkarni, S. R., Hut, P., & McMillan, S. 1993, Nature, 364, 421, doi: 10.1038/364421a0

Lousto, C. O., & Zlochower, Y. 2013, PhRvD, 87, 084027, doi: 10.1103/PhysRevD.87.084027

Maoz, D., Mannucci, F., & Nelemans, G. 2014, ARA&A, 52, 107, doi: 10.1146/annurev-astro-082812-141031

Marín Pina, D., & Gieles, M. 2023, arXiv e-prints, arXiv:2308.10318, doi: 10.48550/arXiv.2308.10318

McMillan, S. L. W. 1986, ApJ, 306, 552, doi: 10.1086/164365

Mikkola, S., & Aarseth, S. J. 1993, Celestial Mechanics and Dynamical Astronomy, 57, 439, doi: 10.1007/BF00695714

Morscher, M., Pattabiraman, B., Rodriguez, C., Rasio, F. A., & Umbreit, S. 2015, ApJ, 800, 9, doi: 10.1088/0004-637X/800/1/9

Morscher, M., Umbreit, S., Farr, W. M., & Rasio, F. A. 2013, ApJL, 763, L15, doi: 10.1088/2041-8205/763/1/L15

O'Leary, R. M., Rasio, F. A., Fregeau, J. M., Ivanova, N., & O'Shaughnessy, R. 2006, ApJ, 637, 937, doi: 10.1086/498446

Peñarrubia, J. 2021, MNRAS, 501, 3670, doi: 10.1093/mnras/staa3700

Quinlan, G. D., & Shapiro, S. L. 1989, ApJ, 343, 725, doi: 10.1086/167745

Rodriguez, C. L., Zevin, M., Amaro-Seoane, P., et al. 2019, PhRvD, 100, 043027, doi: 10.1103/PhysRevD.100.043027

Rodriguez, C. L., Weatherford, N. C., Coughlin, S. C., et al. 2022, ApJS, 258, 22, doi: 10.3847/1538-4365/ac2edf

Rozner, M., Generozov, A., & Perets, H. B. 2023, MNRAS, 521, 866, doi: 10.1093/mnras/stad603

Ryu, T., Perna, R., Pakmor, R., et al. 2023, MNRAS, 519, 5787, doi: 10.1093/mnras/stad079

Sana, H., de Mink, S. E., de Koter, A., et al. 2012, Science, 337, 444, doi: 10.1126/science.1223344

Shu, F. H., Adams, F. C., & Lizano, S. 1987, ARA&A, 25, 23, doi: 10.1146/annurev.aa.25.090187.000323

Statler, T. S., Ostriker, J. P., & Cohn, H. N. 1987, ApJ, 316, 626, doi: 10.1086/165230

Stodolkiewicz, J. S. 1986, AcA, 36, 19

Stoer, J., & Bulirsch, R. 1980, Introduction to Numerical Analysis (Springer-Verlag, New York), 430, doi: https://doi.org/10.1007/978-0-387-21738-3

Tanikawa, A., Heggie, D. C., Hut, P., & Makino, J. 2013, Astronomy and Computing, 3, 35, doi: 10.1016/j.ascom.2013.11.002

Tokovinin, A. 2020, MNRAS, 496, 987, doi: 10.1093/mnras/staa1639

Trani, A. A., Fujii, M. S., & Spera, M. 2019a, ApJ, 875, 42, doi: 10.3847/1538-4357/ab0e70

Trani, A. A., Quaini, S., & Colpi, M. 2023, arXiv e-prints, arXiv:2312.13281, doi: 10.48550/arXiv.2312.13281

Trani, A. A., & Spera, M. 2022, arXiv e-prints, arXiv:2206.10583. https://arxiv.org/abs/2206.10583

Trani, A. A., & Spera, M. 2023, in The Predictive Power of Computational Astrophysics as a Discover Tool, ed. D. Bisikalo, D. Wiebe, & C. Boily, Vol. 362, 404–409, doi: 10.1017/S1743921322001818

Trani, A. A., Spera, M., Leigh, N. W. C., & Fujii, M. S. 2019b, ApJ, 885, 135, doi: 10.3847/1538-4357/ab480a

Wang, L., Spurzem, R., Aarseth, S., et al. 2016, MNRAS, 458, 1450, doi: 10.1093/mnras/stw274

Weatherford, N. C., Kıroğlu, F., Fragione, G., et al. 2023, ApJ, 946, 104, doi: 10.3847/1538-4357/acbcc1

Xu, S., Hwang, H.-C., Hamilton, C., & Lai, D. 2023, ApJL, 949, L28, doi: 10.3847/2041-8213/acd6f7

APPENDIX

Table 1 comprises all the 3BBF probabilities from Figure 10.

Table 1. The 3BBF probabilities from Figure 10 for selected cases of unequal masses, distinguished by hardness and specific mass pairing. Each sub-table contains the values for different minimum hardness ($a_{\rm ij}/a_{\rm fs,ij}$), rows contain probabilities for a specific set of mass ratios (q_1, q_2) with fixed $q_0 = 1$, and columns specify pairing combination. Additionally, the 95% confidence interval is included for every probability. There are exactly 10^9 simulations generated per mass ratio or 2.1×10^{10} in total.

all				
$(q_1, \quad q_2)$	$P_{\rm tot}$	P_{01}	P_{02}	P_{12}
$(0.10, 0.10)$	$(4.05 \pm 0.00) \times 10^{-3}$	$(9.54 \pm 0.02) \times 10^{-4}$	$(9.53 \pm 0.02) \times 10^{-4}$	$(2.14 \pm 0.00) \times 10^{-3}$
$(0.25, 0.10)$	$(7.04 \pm 0.01) \times 10^{-3}$	$(1.04 \pm 0.00) \times 10^{-3}$	$(2.53 \pm 0.00) \times 10^{-3}$	$(3.47 \pm 0.00) \times 10^{-3}$
$(0.40, 0.10)$	$(8.78 \pm 0.01) \times 10^{-3}$	$(1.02 \pm 0.00) \times 10^{-3}$	$(3.60 \pm 0.00) \times 10^{-3}$	$(4.16 \pm 0.00) \times 10^{-3}$
$(0.55, 0.10)$	$(9.64 \pm 0.01) \times 10^{-3}$	$(9.44 \pm 0.02) \times 10^{-4}$	$(4.20 \pm 0.00) \times 10^{-3}$	$(4.49 \pm 0.00) \times 10^{-3}$
$(0.70, 0.10)$	$(9.96 \pm 0.01) \times 10^{-3}$	$(8.60 \pm 0.02) \times 10^{-4}$	$(4.48 \pm 0.00) \times 10^{-3}$	$(4.62 \pm 0.00) \times 10^{-3}$
$(0.85, 0.10)$	$(9.98 \pm 0.01) \times 10^{-3}$	$(7.80 \pm 0.02) \times 10^{-4}$	$(4.57 \pm 0.00) \times 10^{-3}$	$(4.62 \pm 0.00) \times 10^{-3}$
$(1.00, 0.10)$	$(9.82 \pm 0.01) \times 10^{-3}$	$(7.09 \pm 0.02) \times 10^{-4}$	$(4.55 \pm 0.00) \times 10^{-3}$	$(4.55 \pm 0.00) \times 10^{-3}$
$(0.33, 0.33)$	$(1.73 \pm 0.00) \times 10^{-2}$	$(4.82 \pm 0.00) \times 10^{-3}$	$(4.78 \pm 0.00) \times 10^{-3}$	$(7.69 \pm 0.01) \times 10^{-3}$
$(0.44, 0.33)$	$(1.86 \pm 0.00) \times 10^{-2}$	$(4.71 \pm 0.00) \times 10^{-3}$	$(5.80 \pm 0.00) \times 10^{-3}$	$(8.05 \pm 0.01) \times 10^{-3}$
$(0.56, 0.33)$	$(1.90 \pm 0.00) \times 10^{-2}$	$(4.46 \pm 0.00) \times 10^{-3}$	$(6.49 \pm 0.00) \times 10^{-3}$	$(8.07 \pm 0.01) \times 10^{-3}$
$(0.67, 0.33)$	$(1.89 \pm 0.00) \times 10^{-2}$	$(4.19 \pm 0.00) \times 10^{-3}$	$(6.86 \pm 0.01) \times 10^{-3}$	$(7.90 \pm 0.01) \times 10^{-3}$
$(0.78, 0.33)$	$(1.86 \pm 0.00) \times 10^{-2}$	$(3.90 \pm 0.00) \times 10^{-3}$	$(7.03 \pm 0.01) \times 10^{-3}$	$(7.64 \pm 0.01) \times 10^{-3}$
$(0.89, 0.33)$	$(1.81 \pm 0.00) \times 10^{-2}$	$(3.64 \pm 0.00) \times 10^{-3}$	$(7.08 \pm 0.01) \times 10^{-3}$	$(7.36 \pm 0.01) \times 10^{-3}$
$(1.00, 0.33)$	$(1.75 \pm 0.00) \times 10^{-2}$	$(3.39 \pm 0.00) \times 10^{-3}$	$(7.04 \pm 0.01) \times 10^{-3}$	$(7.04 \pm 0.01) \times 10^{-3}$
$(0.50, 0.50)$	$(2.49 \pm 0.00) \times 10^{-2}$	$(7.38 \pm 0.01) \times 10^{-3}$	$(7.38 \pm 0.01) \times 10^{-3}$	$(1.02 \pm 0.00) \times 10^{-2}$
$(0.58, 0.50)$	$(2.51 \pm 0.00) \times 10^{-2}$	$(7.14 \pm 0.01) \times 10^{-3}$	$(7.90 \pm 0.01) \times 10^{-3}$	$(1.01 \pm 0.00) \times 10^{-2}$
$(0.67, 0.50)$	$(2.50 \pm 0.00) \times 10^{-2}$	$(6.84 \pm 0.01) \times 10^{-3}$	$(8.29 \pm 0.01) \times 10^{-3}$	$(9.87 \pm 0.01) \times 10^{-3}$
$(0.75, 0.50)$	$(2.47 \pm 0.00) \times 10^{-2}$	$(6.55 \pm 0.01) \times 10^{-3}$	$(8.50 \pm 0.01) \times 10^{-3}$	$(9.62 \pm 0.01) \times 10^{-3}$
$(0.83, 0.50)$	$(2.42 \pm 0.00) \times 10^{-2}$	$(6.25 \pm 0.00) \times 10^{-3}$	$(8.63 \pm 0.01) \times 10^{-3}$	$(9.33 \pm 0.01) \times 10^{-3}$
$(0.92, 0.50)$	$(2.36 \pm 0.00) \times 10^{-2}$	$(5.92 \pm 0.00) \times 10^{-3}$	$(8.68 \pm 0.01) \times 10^{-3}$	$(8.98 \pm 0.01) \times 10^{-3}$
$(1.00, 0.50)$	$(2.30 \pm 0.00) \times 10^{-2}$	$(5.65 \pm 0.00) \times 10^{-3}$	$(8.67 \pm 0.01) \times 10^{-3}$	$(8.67 \pm 0.01) \times 10^{-3}$

$a_{\rm ij}/a_{\rm fs,ij} < 10$				
$(q_1, \quad q_2)$	$P_{\rm tot}$	P_{01}	P_{02}	P_{12}
$(0.10, 0.10)$	$(3.03 \pm 0.03) \times 10^{-5}$	$(1.41 \pm 0.02) \times 10^{-5}$	$(1.42 \pm 0.02) \times 10^{-5}$	$(1.97 \pm 0.09) \times 10^{-6}$
$(0.25, 0.10)$	$(8.70 \pm 0.06) \times 10^{-5}$	$(1.06 \pm 0.02) \times 10^{-5}$	$(6.78 \pm 0.05) \times 10^{-5}$	$(8.55 \pm 0.18) \times 10^{-6}$
$(0.40, 0.10)$	$(1.34 \pm 0.01) \times 10^{-4}$	$(7.79 \pm 0.17) \times 10^{-6}$	$(1.07 \pm 0.01) \times 10^{-4}$	$(1.89 \pm 0.03) \times 10^{-5}$
$(0.55, 0.10)$	$(1.50 \pm 0.01) \times 10^{-4}$	$(5.53 \pm 0.15) \times 10^{-6}$	$(1.13 \pm 0.01) \times 10^{-4}$	$(3.12 \pm 0.03) \times 10^{-5}$
$(0.70, 0.10)$	$(1.49 \pm 0.01) \times 10^{-4}$	$(3.98 \pm 0.12) \times 10^{-6}$	$(1.01 \pm 0.01) \times 10^{-4}$	$(4.44 \pm 0.04) \times 10^{-5}$
$(0.85, 0.10)$	$(1.43 \pm 0.01) \times 10^{-4}$	$(3.02 \pm 0.11) \times 10^{-6}$	$(8.39 \pm 0.06) \times 10^{-5}$	$(5.63 \pm 0.05) \times 10^{-5}$
$(1.00, 0.10)$	$(1.39 \pm 0.01) \times 10^{-4}$	$(2.34 \pm 0.10) \times 10^{-6}$	$(6.80 \pm 0.05) \times 10^{-5}$	$(6.84 \pm 0.05) \times 10^{-5}$
$(0.33, 0.33)$	$(3.69 \pm 0.01) \times 10^{-4}$	$(1.52 \pm 0.01) \times 10^{-4}$	$(1.50 \pm 0.01) \times 10^{-4}$	$(6.75 \pm 0.05) \times 10^{-5}$
$(0.44, 0.33)$	$(4.08 \pm 0.01) \times 10^{-4}$	$(1.35 \pm 0.01) \times 10^{-4}$	$(1.89 \pm 0.01) \times 10^{-4}$	$(8.44 \pm 0.06) \times 10^{-5}$
$(0.56, 0.33)$	$(4.17 \pm 0.01) \times 10^{-4}$	$(1.18 \pm 0.01) \times 10^{-4}$	$(2.00 \pm 0.01) \times 10^{-4}$	$(9.96 \pm 0.06) \times 10^{-5}$
$(0.67, 0.33)$	$(4.07 \pm 0.01) \times 10^{-4}$	$(1.04 \pm 0.01) \times 10^{-4}$	$(1.92 \pm 0.01) \times 10^{-4}$	$(1.12 \pm 0.01) \times 10^{-4}$
$(0.78, 0.33)$	$(3.90 \pm 0.01) \times 10^{-4}$	$(9.11 \pm 0.06) \times 10^{-5}$	$(1.76 \pm 0.01) \times 10^{-4}$	$(1.23 \pm 0.01) \times 10^{-4}$
$(0.89, 0.33)$	$(3.67 \pm 0.01) \times 10^{-4}$	$(8.05 \pm 0.06) \times 10^{-5}$	$(1.56 \pm 0.01) \times 10^{-4}$	$(1.31 \pm 0.01) \times 10^{-4}$
$(1.00, 0.33)$	$(3.46 \pm 0.01) \times 10^{-4}$	$(7.14 \pm 0.05) \times 10^{-5}$	$(1.37 \pm 0.01) \times 10^{-4}$	$(1.37 \pm 0.01) \times 10^{-4}$
$(0.50, 0.50)$	$(7.05 \pm 0.02) \times 10^{-4}$	$(2.65 \pm 0.01) \times 10^{-4}$	$(2.65 \pm 0.01) \times 10^{-4}$	$(1.76 \pm 0.01) \times 10^{-4}$
$(0.58, 0.50)$	$(7.02 \pm 0.02) \times 10^{-4}$	$(2.46 \pm 0.01) \times 10^{-4}$	$(2.72 \pm 0.01) \times 10^{-4}$	$(1.85 \pm 0.01) \times 10^{-4}$
$(0.67, 0.50)$	$(6.84 \pm 0.02) \times 10^{-4}$	$(2.24 \pm 0.01) \times 10^{-4}$	$(2.68 \pm 0.01) \times 10^{-4}$	$(1.92 \pm 0.01) \times 10^{-4}$
$(0.75, 0.50)$	$(6.62 \pm 0.02) \times 10^{-4}$	$(2.09 \pm 0.01) \times 10^{-4}$	$(2.56 \pm 0.01) \times 10^{-4}$	$(1.96 \pm 0.01) \times 10^{-4}$
$(0.83, 0.50)$	$(6.34 \pm 0.02) \times 10^{-4}$	$(1.93 \pm 0.01) \times 10^{-4}$	$(2.42 \pm 0.01) \times 10^{-4}$	$(2.00 \pm 0.01) \times 10^{-4}$
$(0.92, 0.50)$	$(6.00 \pm 0.02) \times 10^{-4}$	$(1.77 \pm 0.01) \times 10^{-4}$	$(2.21 \pm 0.01) \times 10^{-4}$	$(2.02 \pm 0.01) \times 10^{-4}$
$(1.00, 0.50)$	$(5.69 \pm 0.01) \times 10^{-4}$	$(1.64 \pm 0.01) \times 10^{-4}$	$(2.03 \pm 0.01) \times 10^{-4}$	$(2.03 \pm 0.01) \times 10^{-4}$

Table 1 (Continued)

	$a_{ij}/a_{fs,ij} < 3$			
$(q_1, \quad q_2)$	P_{tot}	P_{01}	P_{02}	P_{12}
$(0.10, 0.10)$	$(1.66 \pm 0.08) \times 10^{-6}$	$(8.21 \pm 0.56) \times 10^{-7}$	$(8.01 \pm 0.56) \times 10^{-7}$	$(4.03 \pm 1.25) \times 10^{-8}$
$(0.25, 0.10)$	$(3.97 \pm 0.12) \times 10^{-6}$	$(6.12 \pm 0.49) \times 10^{-7}$	$(3.18 \pm 0.11) \times 10^{-6}$	$(1.83 \pm 0.27) \times 10^{-7}$
$(0.40, 0.10)$	$(5.34 \pm 0.14) \times 10^{-6}$	$(4.32 \pm 0.41) \times 10^{-7}$	$(4.44 \pm 0.13) \times 10^{-6}$	$(4.66 \pm 0.42) \times 10^{-7}$
$(0.55, 0.10)$	$(5.24 \pm 0.14) \times 10^{-6}$	$(2.75 \pm 0.33) \times 10^{-7}$	$(4.18 \pm 0.13) \times 10^{-6}$	$(7.83 \pm 0.55) \times 10^{-7}$
$(0.70, 0.10)$	$(4.62 \pm 0.13) \times 10^{-6}$	$(1.98 \pm 0.28) \times 10^{-7}$	$(3.27 \pm 0.11) \times 10^{-6}$	$(1.15 \pm 0.07) \times 10^{-6}$
$(0.85, 0.10)$	$(4.26 \pm 0.13) \times 10^{-6}$	$(1.68 \pm 0.26) \times 10^{-7}$	$(2.50 \pm 0.10) \times 10^{-6}$	$(1.59 \pm 0.08) \times 10^{-6}$
$(1.00, 0.10)$	$(3.92 \pm 0.12) \times 10^{-6}$	$(1.25 \pm 0.22) \times 10^{-7}$	$(1.84 \pm 0.08) \times 10^{-6}$	$(1.95 \pm 0.09) \times 10^{-6}$
$(0.33, 0.33)$	$(1.69 \pm 0.03) \times 10^{-5}$	$(7.52 \pm 0.17) \times 10^{-6}$	$(7.50 \pm 0.17) \times 10^{-6}$	$(1.84 \pm 0.08) \times 10^{-6}$
$(0.44, 0.33)$	$(1.75 \pm 0.03) \times 10^{-5}$	$(6.67 \pm 0.16) \times 10^{-6}$	$(8.48 \pm 0.18) \times 10^{-6}$	$(2.36 \pm 0.10) \times 10^{-6}$
$(0.56, 0.33)$	$(1.66 \pm 0.03) \times 10^{-5}$	$(5.80 \pm 0.15) \times 10^{-6}$	$(8.06 \pm 0.18) \times 10^{-6}$	$(2.79 \pm 0.10) \times 10^{-6}$
$(0.67, 0.33)$	$(1.55 \pm 0.02) \times 10^{-5}$	$(5.20 \pm 0.14) \times 10^{-6}$	$(7.17 \pm 0.17) \times 10^{-6}$	$(3.17 \pm 0.11) \times 10^{-6}$
$(0.78, 0.33)$	$(1.44 \pm 0.02) \times 10^{-5}$	$(4.70 \pm 0.13) \times 10^{-6}$	$(6.14 \pm 0.15) \times 10^{-6}$	$(3.58 \pm 0.12) \times 10^{-6}$
$(0.89, 0.33)$	$(1.31 \pm 0.02) \times 10^{-5}$	$(4.10 \pm 0.13) \times 10^{-6}$	$(5.12 \pm 0.14) \times 10^{-6}$	$(3.91 \pm 0.12) \times 10^{-6}$
$(1.00, 0.33)$	$(1.21 \pm 0.02) \times 10^{-5}$	$(3.69 \pm 0.12) \times 10^{-6}$	$(4.15 \pm 0.13) \times 10^{-6}$	$(4.21 \pm 0.13) \times 10^{-6}$
$(0.50, 0.50)$	$(2.94 \pm 0.03) \times 10^{-5}$	$(1.21 \pm 0.02) \times 10^{-5}$	$(1.23 \pm 0.02) \times 10^{-5}$	$(5.07 \pm 0.14) \times 10^{-6}$
$(0.58, 0.50)$	$(2.90 \pm 0.03) \times 10^{-5}$	$(1.16 \pm 0.02) \times 10^{-5}$	$(1.19 \pm 0.02) \times 10^{-5}$	$(5.50 \pm 0.15) \times 10^{-6}$
$(0.67, 0.50)$	$(2.71 \pm 0.03) \times 10^{-5}$	$(1.04 \pm 0.02) \times 10^{-5}$	$(1.09 \pm 0.02) \times 10^{-5}$	$(5.81 \pm 0.15) \times 10^{-6}$
$(0.75, 0.50)$	$(2.57 \pm 0.03) \times 10^{-5}$	$(9.89 \pm 0.20) \times 10^{-6}$	$(9.81 \pm 0.19) \times 10^{-6}$	$(6.02 \pm 0.15) \times 10^{-6}$
$(0.83, 0.50)$	$(2.42 \pm 0.03) \times 10^{-5}$	$(9.23 \pm 0.19) \times 10^{-6}$	$(8.76 \pm 0.18) \times 10^{-6}$	$(6.23 \pm 0.16) \times 10^{-6}$
$(0.92, 0.50)$	$(2.27 \pm 0.03) \times 10^{-5}$	$(8.53 \pm 0.18) \times 10^{-6}$	$(7.63 \pm 0.17) \times 10^{-6}$	$(6.50 \pm 0.16) \times 10^{-6}$
$(1.00, 0.50)$	$(2.13 \pm 0.03) \times 10^{-5}$	$(8.01 \pm 0.18) \times 10^{-6}$	$(6.57 \pm 0.16) \times 10^{-6}$	$(6.69 \pm 0.16) \times 10^{-6}$

	$a_{ij}/a_{fs,ij} < 1$			
$(q_1, \quad q_2)$	P_{tot}	P_{01}	P_{02}	P_{12}
$(0.10, 0.10)$	$(4.63 \pm 1.34) \times 10^{-8}$	$(2.12 \pm 0.90) \times 10^{-8}$	$(2.32 \pm 0.95) \times 10^{-8}$	$(2.02 \pm 2.79) \times 10^{-9}$
$(0.25, 0.10)$	$(1.60 \pm 0.25) \times 10^{-7}$	$(3.02 \pm 1.08) \times 10^{-8}$	$(1.26 \pm 0.22) \times 10^{-7}$	$(4.03 \pm 3.95) \times 10^{-9}$
$(0.40, 0.10)$	$(1.81 \pm 0.26) \times 10^{-7}$	$(1.71 \pm 0.81) \times 10^{-8}$	$(1.49 \pm 0.24) \times 10^{-7}$	$(1.51 \pm 0.76) \times 10^{-8}$
$(0.55, 0.10)$	$(1.86 \pm 0.27) \times 10^{-7}$	$(2.01 \pm 0.88) \times 10^{-8}$	$(1.41 \pm 0.23) \times 10^{-7}$	$(2.52 \pm 0.99) \times 10^{-8}$
$(0.70, 0.10)$	$(1.39 \pm 0.23) \times 10^{-7}$	$(1.21 \pm 0.68) \times 10^{-8}$	$(1.01 \pm 0.20) \times 10^{-7}$	$(2.62 \pm 1.01) \times 10^{-8}$
$(0.85, 0.10)$	$(1.17 \pm 0.21) \times 10^{-7}$	$(4.03 \pm 3.95) \times 10^{-9}$	$(7.35 \pm 1.69) \times 10^{-8}$	$(3.93 \pm 1.23) \times 10^{-8}$
$(1.00, 0.10)$	$(1.20 \pm 0.22) \times 10^{-7}$	$(9.07 \pm 5.92) \times 10^{-9}$	$(5.74 \pm 1.49) \times 10^{-8}$	$(5.34 \pm 1.44) \times 10^{-8}$
$(0.33, 0.33)$	$(5.94 \pm 0.48) \times 10^{-7}$	$(2.56 \pm 0.32) \times 10^{-7}$	$(2.86 \pm 0.33) \times 10^{-7}$	$(5.14 \pm 1.41) \times 10^{-8}$
$(0.44, 0.33)$	$(5.99 \pm 0.48) \times 10^{-7}$	$(2.47 \pm 0.31) \times 10^{-7}$	$(2.97 \pm 0.34) \times 10^{-7}$	$(5.55 \pm 1.47) \times 10^{-8}$
$(0.56, 0.33)$	$(5.48 \pm 0.46) \times 10^{-7}$	$(2.11 \pm 0.29) \times 10^{-7}$	$(2.56 \pm 0.31) \times 10^{-7}$	$(8.07 \pm 1.77) \times 10^{-8}$
$(0.67, 0.33)$	$(5.15 \pm 0.45) \times 10^{-7}$	$(1.95 \pm 0.27) \times 10^{-7}$	$(2.38 \pm 0.30) \times 10^{-7}$	$(8.27 \pm 1.79) \times 10^{-8}$
$(0.78, 0.33)$	$(4.92 \pm 0.44) \times 10^{-7}$	$(1.87 \pm 0.27) \times 10^{-7}$	$(1.82 \pm 0.27) \times 10^{-7}$	$(1.23 \pm 0.22) \times 10^{-7}$
$(0.89, 0.33)$	$(4.35 \pm 0.41) \times 10^{-7}$	$(1.62 \pm 0.25) \times 10^{-7}$	$(1.35 \pm 0.23) \times 10^{-7}$	$(1.37 \pm 0.23) \times 10^{-7}$
$(1.00, 0.33)$	$(3.88 \pm 0.39) \times 10^{-7}$	$(1.31 \pm 0.23) \times 10^{-7}$	$(1.41 \pm 0.23) \times 10^{-7}$	$(1.16 \pm 0.21) \times 10^{-7}$
$(0.50, 0.50)$	$(9.70 \pm 0.61) \times 10^{-7}$	$(4.23 \pm 0.40) \times 10^{-7}$	$(4.11 \pm 0.40) \times 10^{-7}$	$(1.36 \pm 0.23) \times 10^{-7}$
$(0.58, 0.50)$	$(9.49 \pm 0.61) \times 10^{-7}$	$(3.87 \pm 0.39) \times 10^{-7}$	$(4.04 \pm 0.40) \times 10^{-7}$	$(1.57 \pm 0.25) \times 10^{-7}$
$(0.67, 0.50)$	$(8.64 \pm 0.58) \times 10^{-7}$	$(3.93 \pm 0.39) \times 10^{-7}$	$(3.28 \pm 0.36) \times 10^{-7}$	$(1.43 \pm 0.24) \times 10^{-7}$
$(0.75, 0.50)$	$(8.21 \pm 0.56) \times 10^{-7}$	$(3.77 \pm 0.38) \times 10^{-7}$	$(2.74 \pm 0.33) \times 10^{-7}$	$(1.69 \pm 0.26) \times 10^{-7}$
$(0.83, 0.50)$	$(8.18 \pm 0.56) \times 10^{-7}$	$(3.44 \pm 0.37) \times 10^{-7}$	$(2.79 \pm 0.33) \times 10^{-7}$	$(1.95 \pm 0.27) \times 10^{-7}$
$(0.92, 0.50)$	$(7.60 \pm 0.54) \times 10^{-7}$	$(3.42 \pm 0.36) \times 10^{-7}$	$(2.44 \pm 0.31) \times 10^{-7}$	$(1.74 \pm 0.26) \times 10^{-7}$
$(1.00, 0.50)$	$(6.87 \pm 0.52) \times 10^{-7}$	$(2.85 \pm 0.33) \times 10^{-7}$	$(1.92 \pm 0.27) \times 10^{-7}$	$(2.10 \pm 0.29) \times 10^{-7}$